Technische Universität München
Fakultät für Physik

Constraining GRB Afterglow Fireballs with Late Two-Shell Collisions

Wissenschaftliche Arbeit zur Erlangung des Grades B.Sc. Physik
am Max-Planck-Institut für extraterrestrische Physik.

Betreut von PD Dr. rer. nat. habil. Jochen Greiner
Max-Planck-Institut für extraterrestrische Physik

Eingereicht von Elisa Clara Schösser (03688043)

Eingereicht am 25th August 2020

Erstgutachter (Themensteller): PD Dr. rer. nat. habil. Jochen Greiner
Zweitgutachter:

Abstract

Gamma-ray bursts (GRBs) are short and intense flashes of radiation. While the prompt emission spectrum of GRBs peaks in the γ-ray band, the following so called 'afterglow' of GRBs is detected in the X-rays, optical and radio wavelengths. GRBs are most likely resulting from the death of massive stars or the merger of two neutron stars. Their duration is measured in seconds. According to the internal-external shock model, the prompt emission is produced by internal shocks and the afterglow by a shock wave moving into the external medium.

A recent open issue is the origin of an observed rebrightening in some GRB afterglow light-curves. The so called jump component of the GRB light-curve can be explained by the collision of a late ejected blast wave with the forward shock. During the collision, heat energy is produced which is converted into additional radiation. During this thesis, a hydrodynamic model is tested which simulates the collision of two shells and the resulting light-curves. The created light-curves are compared to optical data of GRB 100621A which was observed with GROND. A general parameter study is performed, in which the influence of each parameter describing the characteristics of the shells, the external medium and the physical setting at the shock front on the simulated light-curves is explored. By using the results of the parameter study, it is possible to obtain a precise first estimate for all input parameters of the model, which can be further refined. The best-fit model for the light curve of GRB 100621A yields a χ^2 value of 10.

Contents

List of Figures

1 Introduction

1.1 Gamma ray bursts and their afterglow

After their discovery by military satellites in 1967 (Klebesadel et al., 1973), the origin and mechanism of gamma-ray bursts (GRBs) became an important new research area in astrophysics. With luminosities of up to 10^{54} ergs^{-1} (Frederiks et al., 2013), GRBs are the brightest explosions known in the universe, and thus carry important information about the high-redshift universe.

In order to obtain information about the characteristics and origin of GRBs, their light-curves and spectra are observed and studied. The prompt emission of GRBs peaks in the γ-ray regime and is followed by a broad-band afterglow which can be detected for days or even weeks in the X-ray, optical and radio wavelengths. On average, GRBs occur at a rate of a few per day. Early observations indicated that GRBs are isotropically distributed on the sky. Thus, the first theory that GRBs originate from the galactic center was rejected and the GRB's extragalactic origin could be finally confirmed by measuring their high redshifts of $z = 1$ or more (Metzger et al., 1997).

Gamma-ray bursts can be classified by their duration into short (< 2 s) and long (> 2 s) GRBs (Kouveliotou et al., 1993). Most models of short GRBs assume that their progenitors are compact binary systems consisting of a black hole and a neutron star (BH-NS) or two neutron stars (NS-NS). This theory was confirmed by the joint detection of a gravitational wave (GW 170817) originating from a neutron star merger and a short GRB (Abbott et al., 2017). Although the observation does not prove that all short GRBs originate from the coalescing of two compact objects, at least a fraction do. The first gamma-ray burst associated with a supernova event was GRB 980425 (Galama et al., 1998), but best evidence for the collapsar model was given by the combined measurement of GRB 030329 and the supernova SN 2003dh five years afterwards (Hjorth et al., 2003). During the core collapse or the merger scenario, gravitational energy is released on timescales of milliseconds inside a volume of the order of kilometers cubed (Mészáros, 2006). A fraction of the freed energy is converted into a high temperature fireball consisting of electrons, positrons, photons and baryons and expands relativistically into the external medium (Piran, 1999). In both the binary merger and hypernova scenario, a black hole with a surrounding accretion disk is created which evolves into the central engine of the outburst. The following relativistic explosion creates a relativistic jet of material which is pumped into the external medium. According to the internal-external shock model, the prompt emission of GRBs originates from internal shocks within the created fireball which occur when matter ejected from the central engine at different times collide far from the source. Thus, the prompt emission of a GRB can be described by multiple two-shell collisions. In contrast to the prompt emission, the secondary afterglow originates from the external shock with the circumburst medium which is produced when the fireball starts to decelerate in the external medium. The canonical afterglow can therefore be explained by the collision of one shell with the external medium during which the blast wave's kinetic energy is dissipated and transformed to kinetic energy of the circumburst medium and plasma heat, which is ultimately radiated. Figure 1 shows an artist's impression of this standard fireball model of GRBs.

Most radiation models for GRB afterglows are based on synchrotron emission originating from relativistic electrons which are accelerated in a magnetic field at the forward shock front. Sari et al. (1998) describe the observed emission with a spectrum consisting of four power-law segments

$$F_\nu \propto t^{-\alpha}\nu^{-\beta} \tag{1}$$

with different exponents α and β, t is the observed time after the burst trigger and ν is the frequency (see Fig. 2). The segments are separated by three characteristic break frequencies: the self-absorption frequency ν_a, the typical synchrotron frequency ν_m and the cooling frequency ν_c. Below ν_a, the effects of synchrotron self-absorption are dominant and the medium becomes optically thick. Highly energetic electrons cool more rapidly than less energetic electrons. Above ν_c, the effects of electron cooling become perceivable. Depending on the order of ν_m and ν_c in the spectrum, two different cases are distinguished, the 'fast cooling case' with $\nu_\mathrm{c} < \nu_\mathrm{m}$ is expected at early times and the 'slow cooling case' with $\nu_\mathrm{m} < \nu_\mathrm{c}$ at later times.

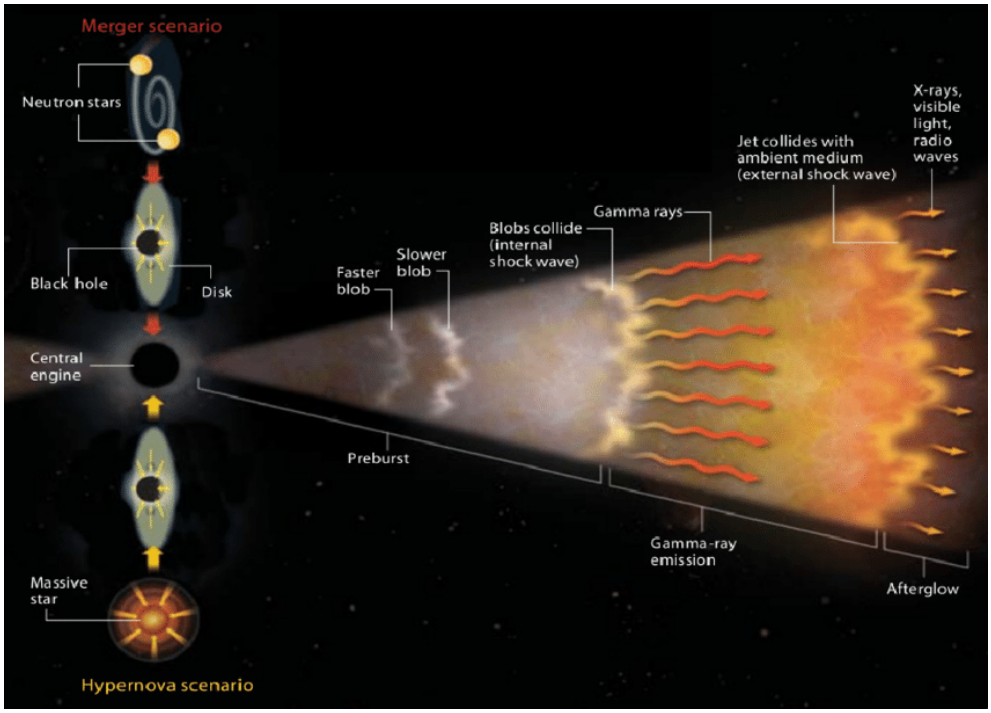

Figure 1: Artist's impression of the standard model of the formation of a GRB. Originating from a hypernova or from the merger of two compact objects (NS-NS or BH-NS), a black hole is formed with a surrounding accretion disk. The central engine blows out a jet of matter into the interstellar medium. While the prompt emission is created via internal shocks within the outflow, the following afterglow is produced by external shocks with the circumburst medium. Figure taken from Gehrels et al. (2002).

The accelerated electrons with random Lorentz factor γ_e at the shock front radius are assumed to have a minimal Lorentz factor γ_m and a power-law distribution with index p,

$$N(\gamma_\mathrm{e}) \propto \gamma_\mathrm{e}^{-p}, \quad \gamma_\mathrm{e} > \gamma_\mathrm{m}. \tag{2}$$

Furthermore, Sari et al. (1998) assume that a fraction ϵ_e of the shock energy is transferred to the accelerated electrons leading to

$$\gamma_\mathrm{m} = \epsilon_\mathrm{e} \frac{p-2}{p-1} \frac{m_p}{m_e} \gamma \tag{3}$$

and that the magnetic energy density is a fraction ϵ_B of the shock energy, giving

$$B = \sqrt{32\pi m_p \epsilon_\mathrm{B} n} \gamma c, \tag{4}$$

where γ denotes the Lorentz factor of the shocked fluid. Here, c is the speed of light, m_p the proton mass and n is the particle density of the external medium. The power P of synchrotron radiation produced by an electron moving with a random Lorentz factor γ_e in a magnetic field with strength B is in the observer frame given by

$$P(\gamma_\mathrm{e}) = \frac{4}{3} \sigma_\mathrm{T} c \gamma^2 \gamma_\mathrm{e}^2 \frac{B^2}{8\pi}, \tag{5}$$

with σ_T the Thomson cross-section. The corresponding emission frequency is

$$\nu(\gamma_\mathrm{e}) = \gamma \gamma_\mathrm{e}^2 \frac{q_\mathrm{e} B}{2\pi m_\mathrm{e} c}, \tag{6}$$

where q_e and m_e are the charge and mass of the electron respectively. The hydrodynamics are described in this model by the self-similar Blandford & McKee (Blandford & McKee, 1976) solution.

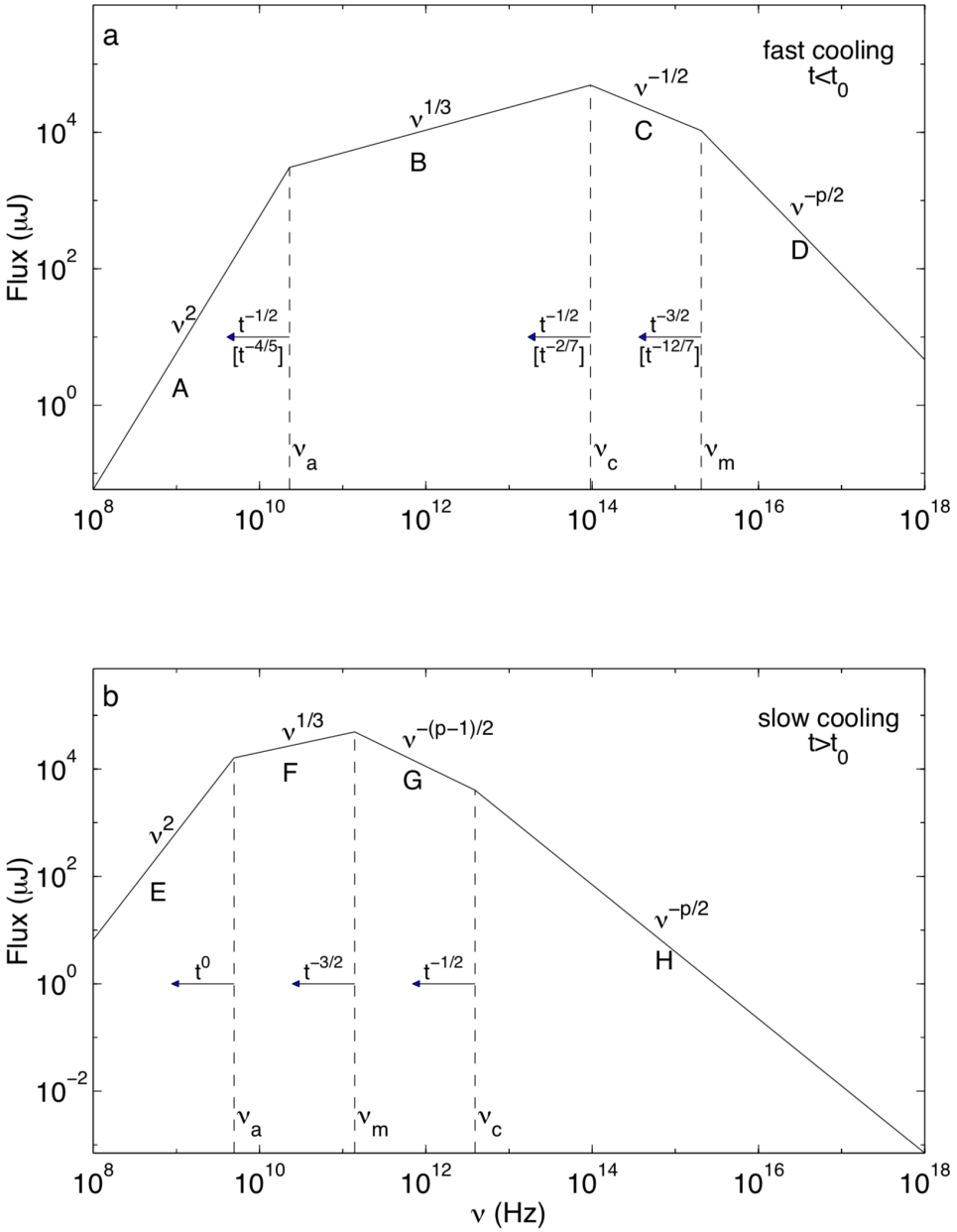

Figure 2: Model of a synchrotron spectrum created by electrons in a relativistic shock that have a power law energy distribution with index p. The four power-law segments are separated by the three break frequencies ν_a, ν_m and ν_c. (a) Fast cooling case, which is expected at early times. For the adiabatic evolution, the change of the break frequencies with time is indicated above the arrows and for the fully radiative case in squared brackets underneath the arrows. (b) Slow cooling case, which is expected at late times and in which the evolution is always adiabatic. Figure taken from Sari et al. (1998).

The blast wave propagates into an external medium with density

$$\rho_{\rm ext} = m_{\rm p} n \left(\frac{R}{R_{\rm ref}} \right) r^{-k}, \tag{7}$$

where $m_{\rm p}$ is the proton mass and n the normalized particle density at radius $R_{\rm ref}$. The case with $k = 0$ corresponds to an interstellar medium (ISM) with constant density, and $k = 2$ to an external medium which is dominated by the progenitor's strong wind. For both external medium cases, under the assumption that radiative losses are small and for different chronological orders of the break frequencies, Granot & Sari (2002) give a full and detailed description of all possible spectra (see Appendix B). The flux density is calculated by integrating over all contributions of created photons which reach the observer from the shocked region. Observations of the broad-band spectra of GRBs always aim to measure all break frequencies and their evolution. This measurement requires observations from different telescopes in different wavelengths to overlap in time which is not often possible. The comparison of observed spectra and light-curves to emission models can determine many of the microphysical parameters used to explain the formation of a GRB.

A current open issue is the measurement of late rebrightenings in GRB light-curves (Nardini et al., 2011; Greiner et al., 2013; Nardini et al., 2014). One explanation of the sudden late flux increase is the collision of a late ejected shell with an earlier ejected shell which is decelerating into the external medium. During this thesis, a hydrodynamic model created by Philip Straub was tested (Straub, 2019). The fully adiabatic model is coupled to a radiation code (van Eerten, 2010; van Eerten et al., 2012) to simulate the resulting light-curves. The produced light-curves are compared to data of GRB 100621A which was observed with the Gamma-ray Burst Optical/Near-infrared Detector (GROND). A parameter study is performed to obtain physical parameters describing the formation of the GRB.

1.2 Multi-wavelength observations of GRB 100621A

The aim of broad-band GRB observations is always to measure the full synchrotron spectrum at different times after the trigger in order to obtain all break frequencies and their evolution. As the spectrum is changing with time, it is important to take spectra with instruments in different wavelength regimes simultaneously, which can be very challenging. Up until now, the identification of all break frequencies and their evolution from measured spectra has been possible for only a handful of GRBs. By obtaining the full synchrotron spectrum at different times and by comparing it to a model as the one of Granot & Sari (2002), it is possible to determine the corresponding six microphysical parameters: the kinetic energy of the blast wave E_1, the shape of the external medium described by k, the density of the external medium n normalized by $R_{\rm ref}$, the spectral index p and the fraction of energy imparted to the magnetic field $\epsilon_{\rm B}$ and to the electrons $\epsilon_{\rm e}$. Furthermore, the model of Granot & Sari (2002) is only applicable when the redshift z of the GRB is measured which is primarily determined by absorption spectroscopy of the GRB's optical afterglow. GRB 100621A was one of the only GRBs for which the redshift z was obtained and comprehensive broad-band observations were performed, especially in the optical wavelengths with GROND (Greiner et al., 2008). The full data set of GRB 100621A was analyzed and presented in Greiner et al. (2013).

The Burst Alert Telescope (BAT) on the Swift satellite (Gehrels et al., 2004) was triggered by GRB 100621A on June 21, 2010 at 03:03:32 UT (Ukwatta et al., 2010). The bright prompt emission was detected for 70 s and after 76 s, the X-Ray Telescope (XRT) and UltraViolet and Optical Telescope (UVOT) on board the Swift satellite began to take data. GRB 100621A had the brightest X-ray afterglow of all observed GRBs so far. From a spectrum taken with X-Shooter at the Very Large Telescope (VLT), a redshift of $z = 0.542$ was obtained (Milvang-Jensen et al., 2010). In a flat universe with $H_0 = 69.6$ kms^{-1}Mpc^{-1}, $\Omega_{\rm M} = 0.286$ and $\Omega_\Lambda = 0.714$, the redshift corresponds to a luminosity distance of $D_{\rm L} = 9.74 \times 10^{27}$ cm. Additional observations with Konus-WIND and the INTErnational Gamma-Ray Astrophysics Laboratory (INTEGRAL) allowed for measurements of a time-integrated spectrum, from which an isotropic energy release of $E_{\rm iso} = (2.8 \pm 0.3) \times 10^{52}$ erg

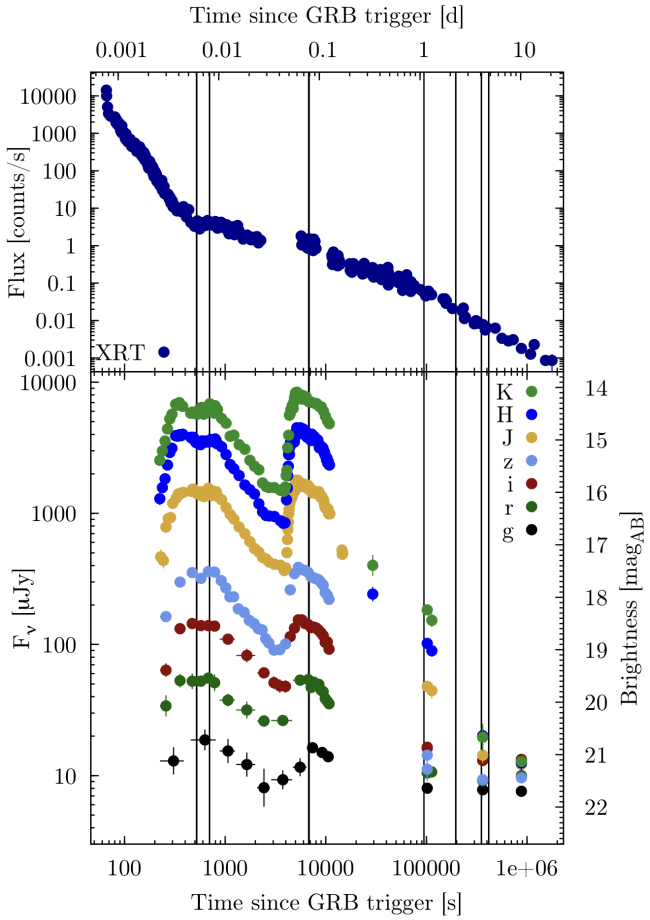

Figure 3: X-ray (top) and optical (bottom) afterglow light-curves of GRB 100621A as observed with Swift and GROND in its seven bands ($g'r'i'z'JHK_s$). The vertical lines depict the times at which spectral energy distributions were measured. Figure taken from (Greiner et al., 2013).

was determined (Golenetskii et al., 2010). Furthermore, observations with the Atacama Pathfinder Experiment (APEX) and the Australia Telescope Compact Array (ATCA) in radio wavelengths were performed. Spectral energy distributions (SEDs) measured with GROND revealed a strong host extinction of $A_V = 3.6$ mag (Krühler et al., 2011) which had to be corrected for in the data used during the thesis.

The optical light-curve used during this thesis was observed with GROND, a simultaneous seven-channel optical/ near-infrared imager which is located at La Silla in Chile (Greiner et al., 2008). The telescope is operated by the Max-Planck-Gesellschaft (MPG) and the European Southern Observatory (ESO). GROND allows simultaneous imaging in four optical ($g'r'i'z'$) and three near-infrared bands (JHK_s). A 3.05 hrs long exposure of GRB 100621A with GROND started automatically 230 s after the GRB was triggered by Swift (Updike et al., 2010). More observations with GROND were made during nights 2, 4 and 10 after the Swift trigger. The X-ray afterglow light-curve of GRB 100621A as observed by Swift and the optical light-curves measured with GROND in its seven filter bands are shown in Figure 3. Approximately one hour after the prompt emission, a late rebrightening in the light-curve was measured in all seven optical bands of GROND. This sudden flux increase is not visible in the X-rays. In the following, the sudden jump in flux is called the jump component of the GRB and is explained by the two-shell collision model constructed in previous work by Straub (2019). The comprehensive observations of GRB 100621A, especially the extensive measurements in the optical regime with GROND (Greiner et al., 2008), make the GRB a perfect probe for testing the created two-shell collision model.

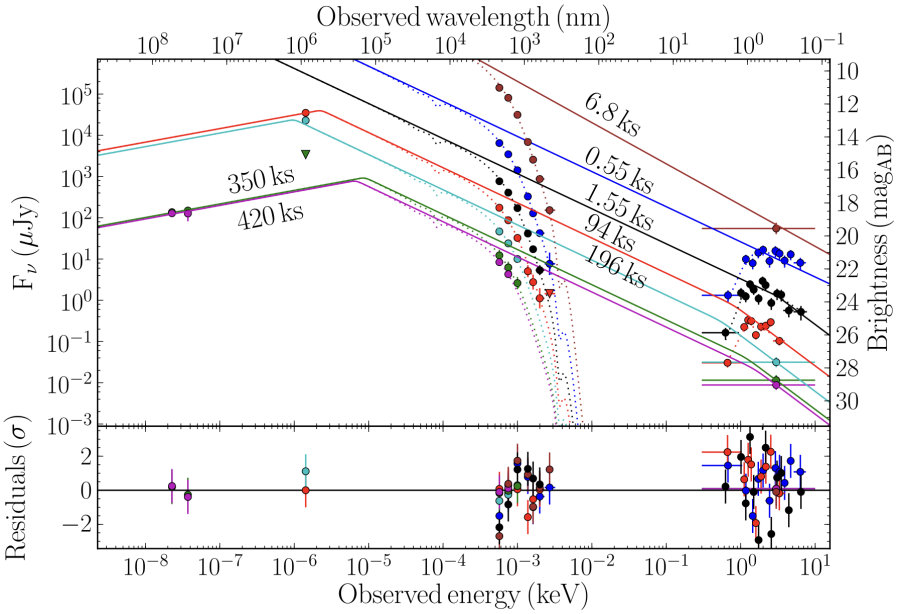

Figure 4: Spectral energy distributions (SEDs) of GRB 100621A which were measured at different times indicated by different colors. The times at which the SEDS were measured are marked with vertical lines in Figure 3. Radio data (on the left) was measured with APEX and ATCA, optical data (in the middle) with GROND, X-ray data (on the right) with Swift. The curvature of the GROND and Swift data is due to strong host extinction (indicated by dotted lines), which has to be corrected for in the measured light-curves. For each time interval, a model which fits to all data points is shown with continuous lines in the corresponding color. Figure taken from Greiner et al. (2013).

From the beginning of the observations with GROND to around 400 s, the optical light-curve rises rapidly. Between 400 and 700 s after the burst, the light-curve becomes almost flat which is likely due to flares. From about 700 to 3000 s, the flux decreases and after a short flattening, a steep rise in flux $F \propto t^{14}$ (Greiner et al., 2013) was measured between 5 and 6 ks. The intensity jump is larger in the NIR bands than in the optical and is not visible in the X-rays (see Fig. 3). Following the intensity jump, the flux decreases at first slowly between 5 and 9 ks and then decays steeply until after 10^5 s, the light-curve flattens to reveal the flux of the host galaxy of the GRB.

In Figure 4, the measured SEDs at different times are shown. The data set which was measured at a specific time is indicated by the same color. The times at which the SEDs were measured are marked by vertical lines in Figure 3. The optical data observed with GROND is not A_V corrected and thus, appears as curved. For each time, a synchrotron model which fits to all data points is shown with continuous lines. Initially, the spectrum measured in the first 1 ks with GROND was fit independently with a power-law function $F \propto \nu^{-\beta}$ which yielded a best-fit spectral slope of $\beta = 0.8 \pm 0.1$ (Greiner et al., 2013). By comparing the result to the theoretical predictions of Granot & Sari (2002) (see Appendix B), the fast cooling case (spectrum 4 and 5) could be excluded at any time because the measured spectral slope is larger than the predicted slope of $\beta = 0.5$ for the fast cooling case (as shown in Figure 2a). While for spectra taken at early times after the Swift trigger, a single power law fit is sufficient for the combined X-ray and optical data, for later measured SEDs, a spectral break in between the X-ray and optical data has to be introduced. As the measured slope difference of 0.6 ± 0.2 between the new power law segments is consistent with the predicted 0.5, the spectral break is identified as the cooling frequency ν_c (see Figure 2a). That the spectral break ν_c only occurs in SEDs measured at later times and that the spectral slope of the SEDs in X-rays steepens with time, is consistent with the theory that ν_c moved from higher to lower energies, which is only the case for an ISM with a constant density circumburst medium ($k = 0$). The corresponding electron spectral index is $p = 2.62 \pm 0.04$. The radio data observed

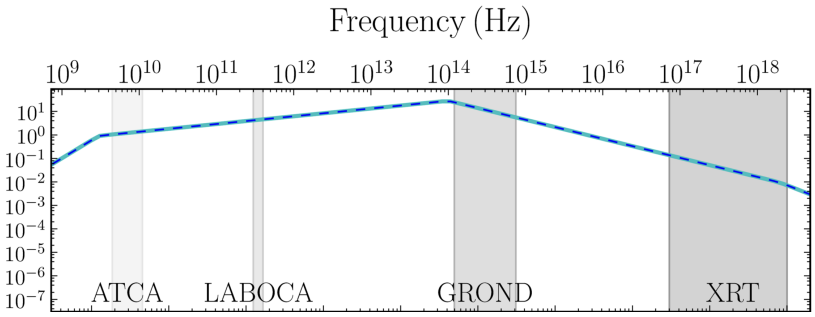

Figure 5: Best fit spectral energy distribution of the canonical afterglow of GRB 100621A (y-axis in units of mJy). The frequency regimes which were covered by the different observations are colored in grey. The optical data observed with GROND has the same spectral slope as the X-ray data observed with XRT. Figure taken from Greiner et al. (2013).

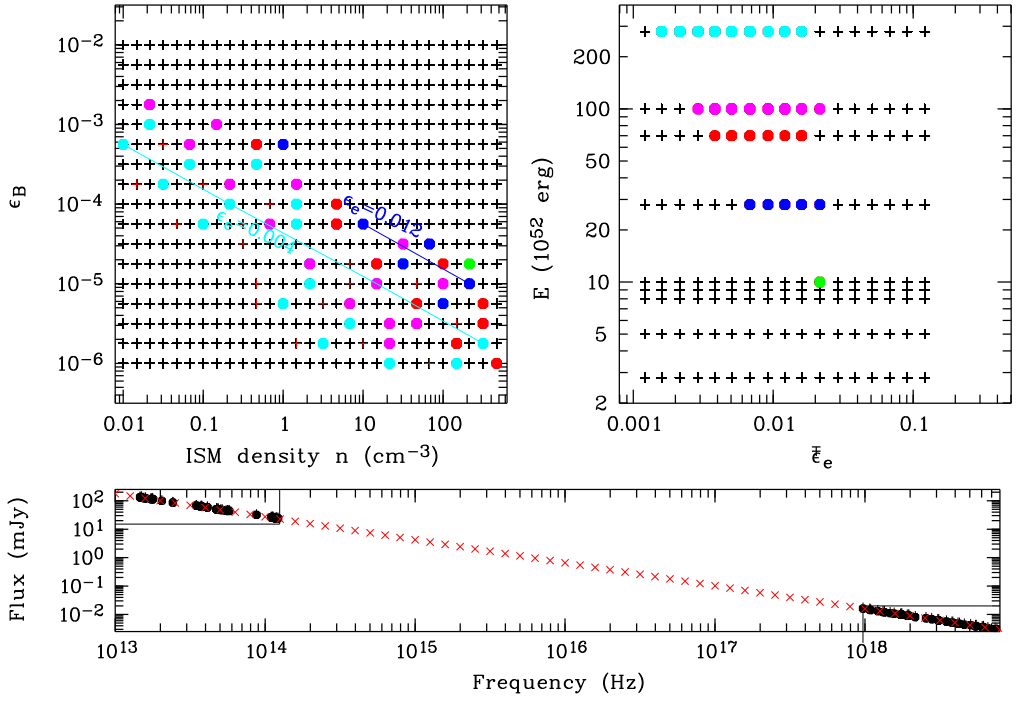

Figure 6: Constraints on the parameters describing the microphysical setting at the front of the external shock originating from the best-fit spectrum. Points on the grid, which fulfill the five constraints mentioned in the text, are marked with circles. Colors correspond to a specific kinetic energy. Adapted figure from Greiner et al. (2013).

with ATCA implies that the self absorption frequency has to be smaller than 5.5 GHz, which leaves 'spectrum 1' from Granot & Sari (2002) as the only option to describe the observed SED. The best fit spectrum for the canonical afterglow is depicted in Figure 5.

The comparison of the observed spectrum to 'spectrum 1' of Granot & Sari (2002) provides four constraints on the break frequencies ν_c and ν_m and the corresponding flux,

1) $\nu_c > 4$ keV,
2) $\nu_m < 10^{14}$ Hz,
3) $F(\nu_c) < 35\ \mu$Jy,
4) $F(\nu_m) > 9$ mJy,

Using the equations in line 2 and 3 of Table 2 of Granot & Sari (2002) and the measured value $p = 2.62 \pm 0.04$, the constraints yield the following four conditions,

1) $\epsilon_B^{-3/2} n^{-1} E_{52}^{-1/2} > 2.82 \times 10^4$,
2) $\bar{\epsilon_e}^2 \epsilon_B^{1/2} E_{52}^{1/2} < 6.46 \times 10^{-6}$,
3) $\bar{\epsilon_e}^{1.62} \epsilon_B^{2-12} n^{1.31} E_{52}^{1.81} < 7.17 \times 10^{-9}$,
4) $\epsilon_B^{1/2} n^{1/2} E_{52} > 0.195$,

where n is in units of cm^{-3}, $\bar{\epsilon_e} = (p-2)/(p-1)\epsilon_e$ and E_{52} is in units of 10^{52} erg. As a fifth condition, which was added during this thesis, the flux density of $F(\nu_c)$ and $F(\nu_m)$ have to lie on the same power law with $\beta = 0.8 \pm 0.1$ as shown in Figure 5. All combined constraints for the microphysical parameters from the canonical afterglow are shown in Figure 6. A grid of points was created and the points of the grid which fulfill all five constraints are marked with circles. The different colored circles belong to a specific kinetic energy E. As a result, for one specific energy, there are always infinitely many possible combinations of n, ϵ_B and ϵ_e, which all have a similar light-curve as a result. Thus, the parameters n, ϵ_B and ϵ_e are ambiguous and cannot be independently determined.

2 Theoretical framework

This Chapter contains the theoretical framework of the model constructed by Straub (2019). In the first part, the most important equations of relativistic hydrodynamics are summarized and in the second part, it is explained how the relativistic hydrodynamics theory is used to create a model which can explain the late rebrightenings in the optical light-curves. All simplifications required to create efficient simulations are fully detailed.

2.1 Relativistic hydrodynamics

To describe the properties of the relativistic blast wave, the external shock (between the relativistic ejecta and the interstellar medium) and the shock produced when two shells collide, relativistic hydrodynamics is needed. In the following, a locally Minkowski metric with natural units ($c = 1$) is used,

$$\eta^{\mu\nu} = \mathrm{diag}(1, -1, -1, -1). \tag{8}$$

The 4-velocity is defined as

$$u^\mu := \frac{dx^\mu}{d\tau}, \tag{9}$$

with τ the fluid proper time and $x^\mu = (t, x^i)$. The metric signature requires that

$$u^\mu u_\mu = 1. \tag{10}$$

The derivative of the coordinate time with respect to the proper time is the Lorentz factor γ, from which the 4-velocity may be written as

$$u^\mu = \gamma \begin{pmatrix} 1 \\ \vec{\beta} \end{pmatrix} \tag{11}$$

with $\vec{\beta}$ the velocity vector.

2.1.1 Perfect relativistic fluids

In the model created by Straub (2019), all hydrodynamic calculations are based on the motion of perfect relativistic fluids. For perfect fluids, an inertial reference frame exists, in which the fluid is isotropic. In this so-called local rest frame, the fluid velocity 4-vector can be written (with $c = 1$) as

$$u^\mu = (1, \vec{0})^T. \tag{12}$$

In general, the energy-momentum tensor is defined as

$$T^{\mu\nu} = (e + p)u^\mu u^\nu - p\eta^{\mu\nu}. \tag{13}$$

Perfect fluids are only characterized by their density and pressure. For perfect relativistic fluids, the energy-momentum tensor is diagonal in the local rest frame,

$$T^{\mu\nu} = \begin{pmatrix} e & 0 & 0 & 0 \\ 0 & p & 0 & 0 \\ 0 & 0 & p & 0 \\ 0 & 0 & 0 & p \end{pmatrix}, \tag{14}$$

with p the pressure of the fluid and e the energy density in the local rest frame, as in Rezzolla & Zanotti (2013). Viscous effects and heat fluxes are zero for perfect fluids. The mass flux in the μ direction is defined by

$$J^\mu = \rho u^\mu. \tag{15}$$

The relativistic motion of a perfect fluid can be obtained from the relativistic hydrodynamic equation, namely the conservation of rest mass,

$$\partial_\mu(J^\mu) = \partial_\mu(\rho u^\mu) = 0 \tag{16}$$

and the conservation of energy and momentum,

$$\partial_\mu T^{\mu\nu} = \partial_\mu \left[(e+p)u^\mu u^\nu - p\eta^{\mu\nu}\right] = 0, \tag{17}$$

which yield five equations (mass conservation, energy conservation for $\mu = 0$ and momentum conservation for $\mu = 1, 2, 3$) for six unknowns, the three components of the 4-velocity (the fourth component is determined by the normalization condition in equation 10), the mass density ρ, the pressure p and the energy density e. A sixth equation is given by the equation of state,

$$p = (a-1)(e-\rho), \tag{18}$$

where a is the adiabatic index, which equals 4/3 for a hot and 5/3 for a cold fluid. Furthermore, the relativistic specific enthalpy is defined as

$$h := \frac{e+p}{\rho} \tag{19}$$

and the local rest frame enthalpy density is defined as

$$w := h\rho = e + p \tag{20}$$

2.1.2 Shock waves and contact discontinuities

A discontinuity represents a surface which separates two regions of a fluid with an abrupt change of one or more fluid parameters which propagates with a velocity in excess of the speed of sound. A shock wave separates the space into two regions. The region ahead of the shock is termed 'upstream', and the region behind 'downstream'. At the location of the shock, the hydrodynamic equations are not applicable and are replaced by the so-called Rankine-Hugoniot junction conditions (see e.g. Taub (1948) for the special relativistic case), which demand that rest-mass flux, energy and momentum are conserved across the discontinuity, e.g.

$$J = \rho_a \gamma_a u_a = \rho_b \gamma_b u_b, \tag{21}$$

$$\rho_a h_a \gamma_a^2 u_a^2 + p_a = \rho_b h_b \gamma_b^2 u_b^2 + p_b, \tag{22}$$

$$\rho_a h_a \gamma_a^2 u_a = \rho_b h_b \gamma_b^2 u_b, \tag{23}$$

where J is the rest mass density current projected on the plane perpendicular to the shock and γ_a and γ_b the Lorentz factors of the fluid on side a and b of the shock respectively (Rezzolla & Zanotti, 2013). From the junction conditions, it is possible to compute the velocity on both sides of the shock from the fluid parameters by

$$\beta_a^2 = \frac{(p_a - p_b)(e_b + p_a)}{(e_a - e_b)(e_a + p_b)} \tag{24}$$

$$\beta_b^2 = \frac{(p_a - p_b)(e_a + p_b)}{(e_a - e_b)(e_b + p_a)}, \tag{25}$$

from which the relative velocity of both fluids is given by

$$\beta_{ab} = \frac{\beta_a - \beta_b}{1 - \beta_a \beta_b} = \sqrt{\frac{(p_a - p_b)(e_a - e_b)}{(e_a + p_b)(e_b + p_a)}}. \tag{26}$$

Contact discontinuities are a special case of shock waves with no mass flux across the discontinuity ($J = 0$). Both separated zones are in pressure equilibrium, i.e. $p_a = p_b$.

2.1.3 The Riemann problem for two colliding shells

The Riemann problem is a boundary value problem. The initial fluid parameters on the left and right side of an imaginary layer at time $t = 0$ are given by the state vectors

$$\psi_{\mathrm{L}} = \begin{pmatrix} \rho_{\mathrm{L}} \\ e_{\mathrm{L}} \\ \beta_{\mathrm{L}} \end{pmatrix} , \psi_{\mathrm{R}} = \begin{pmatrix} \rho_{\mathrm{R}} \\ e_{\mathrm{R}} \\ \beta_{\mathrm{R}} \end{pmatrix} , \tag{27}$$

where the valid regions of the state vectors are

$$\psi^0(x) = \begin{cases} \psi_{\mathrm{L}} & \text{if } x < 0 \\ \psi_{\mathrm{R}} & \text{if } x > 0 \end{cases} . \tag{28}$$

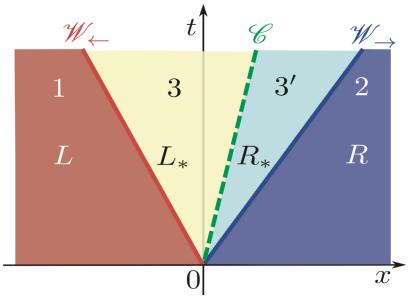

Figure 7: Spacetime diagram of the four regions of the Riemann problem. In the case of two colliding shells, region 3 and 3' are separated by a contact discontinuity. Between regions 1 and 3 there is a shock wave, as between 2 and 3'. Figure taken from Rezzolla & Zanotti (2013)

For a collision to occur, i.e. to obtain a shock-shock scenario, the velocity of the second shell β_{L} has to be greater than the velocity of the first shell β_{R}. When two shells collide at $t = 0$, the fluid is divided into four different regions, which are separated by three different discontinuities (see Figure 7). Each region has a constant density vector and is characterized by the following:

- Region 1: The state vector is described by the original state ψ_{L}.
- Region 2: The state vector is described by the original state ψ_{R}.
- Region 3 is separated from region 1 by a shock. The state vector is unknown.
- Region 3' is separated from region 3 by a contact discontinuity ($p_3 = p_{3'}$, $\beta_3 = \beta_{3'}$) and from region 2 by a shock. The state vector is also unknown.

In the following, the jump conditions (Equations (21 - 23)) are used to compute the unknown fluid quantities for every region. As the regions are propagating with different velocities, the boundaries are defined by the relative velocities between them. By using Equations (24) and (25), the velocities can be calculated as a function of the known fluid properties. In addition, it can be used that the velocities of the fluids which are separated by a contact discontinuity are the same. The exact solution of the one-dimensional Riemann problem for the fluid parameters and their velocities for all regions was taken from Lora-Clavijo et al. (2013).

2.1.4 Relativistic blast waves

Produced by a central engine after an impulsive burst of high energy, blast waves are very rapid flows propagating into a cold medium at rest. Blast waves can be described as highly relativistic homogeneous and spherically symmetric thin shells. The hydrodynamic properties of such a blast wave are shown in Figure 8 (Straub, 2019). The blast wave creates a shock which separates it from the external medium. The shock front propagates with Lorentz factor Γ.

The fluid parameters of the external medium are all dependent on the external density ρ_{ext} and are given by

$$\rho_{\text{ext}} = \rho_{\text{ext}}(r) \propto r^{-k}, \tag{29}$$
$$e_{\text{ext}} = (1+\epsilon)\rho_{\text{ext}}, \tag{30}$$
$$p_{\text{ext}} = (a-1)\epsilon\rho_{\text{ext}}, \tag{31}$$
$$w_{\text{ext}} = (1+a\epsilon)\rho_{\text{ext}} = h\rho_{\text{ext}}, \tag{32}$$
$$\beta_{\text{ext}} = 0. \tag{33}$$

The fluid parameters behind the shock (subscript b) characterizing the blast wave can be computed by using the junction conditions (Equations (21 - 23)) and using $\rho_a = \rho_{\text{ext}}(r)$, which yield in the local rest frame

$$\rho_b = 2\sqrt{2}\Gamma^2 h\rho_a, \tag{34}$$
$$e_b = 2\Gamma^2 w_a = 2\Gamma^2 h\rho_a, \tag{35}$$
$$p_b = \frac{2}{3}\Gamma^2 w_a = \frac{2}{3}\Gamma^2 h\rho_a, \tag{36}$$
$$w_b = \frac{8}{3}\Gamma^2 w_a = \frac{8}{3}\Gamma^2 h\rho_a, \tag{37}$$
$$\gamma_b = \frac{\Gamma}{\sqrt{2}}, \tag{38}$$

as in Blandford & McKee (1976).

The first component of the energy-momentum tensor (Equation (13)) and of the current density (Equation (15)) are approximately given by

$$\epsilon_{\text{b}}^0 \approx w_b\gamma_b^2 = \frac{4}{3}\Gamma^4 h\rho_a, \tag{39}$$
$$\mu_b \approx 2\Gamma^2\rho_a, \tag{40}$$

which correspond to the energy and mass density of the blast wave respectively. The global energy and mass conservation is given by

$$E_b = E_0 + \Delta E, \tag{41}$$
$$M_b = M_0 + \Delta M, \tag{42}$$

where ΔE and ΔM are the energy and mass collected by the blast wave from the external medium. The collected mass can be computed as the integral over the density of the external medium,

$$\Delta M := m(R) = 4\pi\int_0^R \rho_{\text{ext}} r^2 dr. \tag{43}$$

By assuming that the shell is homogeneous, the energy and the mass of the blast wave can be calculated by

$$E_b = \epsilon_{\text{b}}^0 \cdot V = \frac{4}{3}\Gamma^4 h\rho_a \cdot V = E_0 + \Delta E, \tag{44}$$
$$M_b = \mu_b \cdot V = 2\Gamma^2\rho_a \cdot V = M_0 + m. \tag{45}$$

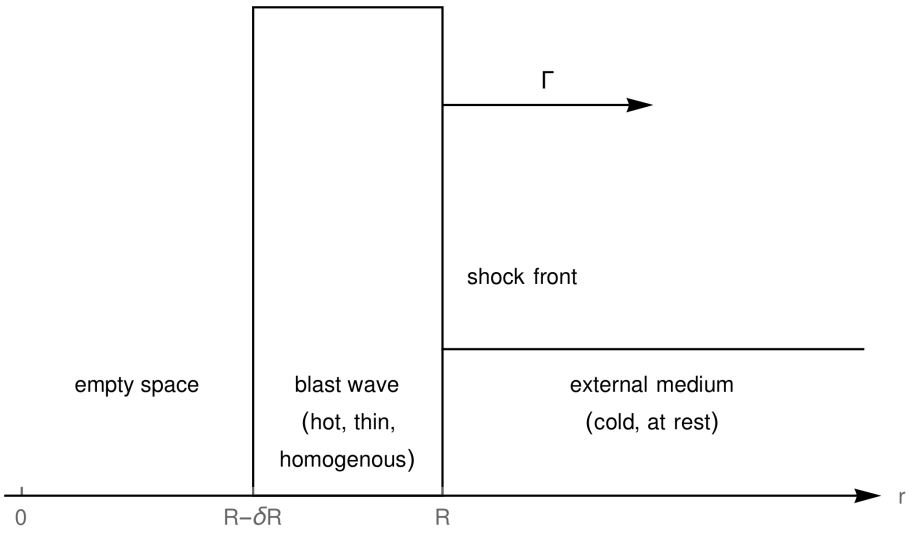

Figure 8: Characteristics of a relativistic blast wave propagating into a cold external medium. The y-axis shows the density of the different regions. Figure taken from Straub (2019).

By dividing E_b by M_b, one obtains

$$\frac{E_b}{M_b} = \frac{2}{3}\Gamma^2 h = \frac{E_0 + \Delta E}{M_0 + \Delta M}, \tag{46}$$

which yields with $E_0 \gg \Delta E$ in the case of relativistic motion an equation for Γ as a function of the radius R,

$$\Gamma^{-2} = \frac{2h}{3E_0}(M_0 + \Delta M) = \Gamma_{\mathrm{i}}^{-2} + \frac{2hm(R)}{3E_0}, \tag{47}$$

with $\Gamma_{\mathrm{i}} := (3E_0/(2hM_0))^{1/2}$ the initial Lorentz factor. The equation can be solved numerically to obtain $R(t)$. During this thesis, another approach was used to derive the evolution of the shock front radius, which is explained in Section 3.1. Under the same assumption, that $E_0 \gg \Delta E$, the volume of the blast wave is given by

$$V = \frac{E_b}{\epsilon_{\mathrm{b}}^0} \approx \frac{3E_0}{4h\rho_a\Gamma^4} = \frac{3E_0}{4h\rho_a}\left(\Gamma_{\mathrm{i}}^{-2} + \frac{2hm}{E_0}\right)^2, \tag{48}$$

from which the width of the shell ΔR can be estimated by using

$$\Delta R \approx \frac{V}{4\pi R^2}. \tag{49}$$

2.2 The two-shell collision model

In the previous work by Straub (2019) two hydrodynamic models were created and coupled to the radiation code of van Eerten (2010); van Eerten et al. (2012). In the first model, only one blast wave propagates into a cold interstellar medium and the produced radiation is simulated. In the second model, the propagation of a second shell ejected later by the central engine is added, which propagates into empty space with constant Lorentz factor as the first shell sweeps up all the circumburst medium. As the first blast wave slows down because of the interaction with the interstellar medium, the second shell collides with the first blast wave.

For $r > R$ with R the radius of the blast wave, the hydrodynamic properties of the external medium are given by Equations (29) to (33). The first blast wave (in the region $R - \Delta R < r < R$)

decelerating into the external medium is characterized by the fluid properties of Equations (34) to (38). Behind the first blast wave in empty space, all fluid parameters become zero. The second shell is described by its energy E_2, width ΔR_2, mass M_2 and Lorentz factor Γ_2 and is cold ($E_2 = \Gamma_2 M_2$). As the second shell propagates into empty space, there are no interactions and thus, E_2, ΔR_2, M_2 and Γ_2 are constant parameters. The fluid Lorentz factor is equal to Γ_2. The equation of state is given by Equation (18) as $p = (a-1)(e-\rho)$ with $a = 5/3$ for a cold fluid. The first component of the rest mass density current (equation 53) corresponds to the mass density $\mu = \rho_2\Gamma_2$ and equals M_2/V_2. Similarly, the energy density can be calculated from the zeroth component of the energy momentum tensor (Equation (13)) and by using $\epsilon_2 = E_2/V_2$, which yields

$$\epsilon_2 = (e_2 + p_2)\Gamma_2^2 - p_2, \tag{50}$$

where p_2 can be related to the density ρ_2 by the equation of state. Additionally, the density ρ_2 can be calculated by

$$\rho_2 = \frac{M_2}{\Gamma_2 V_2}. \tag{51}$$

All fluid parameters of the second shell are thus determined.

The fluid parameters of the colliding shells in the region $R-\Delta R-\Delta R_2 < r < R$ are given by solving the one dimensional Riemann Problem. The rebrightening in the light-curve can be explained by the heat energy E_{heat} which is produced during the collision time and which is converted into radiation. During the collision, the evolution of the first shell and any boundary effects originating from the finite width of the shells are neglected. After the forward shock crosses the first shell, the following evolution is described by one combined shell which has mass, energy and momentum equal to the respective sum of the two individual shells. The radiative losses during the deceleration of the first shell, in which a part of the energy is converted into radiation, is neglected.

A similar but more complex, fully numerical model simulating the late collision of two blast waves in late afterglows was created by Vlasis et al. (2011). The comparison between the model created by Straub (2019) and Vlasis et al. (2011) is further explored in Section 4.2.

3 Modification of the theory

In order to apply the theoretical model developed by Straub (2019) to observed data, some theoretical modifications had to be implemented, which are presented in the following sections. While in Straub (2019), the evolution of the blast waves was calculated numerically, during this thesis the analytical Blandford & McKee solution is used (Blandford & McKee, 1976). Furthermore, it is described how the heat energy can be calculated explicitly.

3.1 Evolution of relativistic blast waves

When examining the evolution of a blast wave, two cases for the circumburst medium have to be considered separately. In the first case, the blast wave propagates into an interstellar medium (ISM) with constant density ($k = 0$) and in the second case, the blast wave propagates into a wind medium ($k = 2$) (Panaitescu & Kumar, 2000). If the GRB was produced during the merging of two compact objects, it is expected that the circumburst medium is homogeneous. If the origin of the GRB is the collapse of a massive star instead, the circumburst medium is characterized by the wind ejected by the prior star. The density of this wind profile medium decreases with increasing distance R from the center as $\rho_{\text{ext}} \propto R^{-2}$. The two cases for the density profile of the external medium can be described by Equation 7.

Immediately after the ejection of the extremely hot fireball, the shell's Lorentz factor Γ increases linearly with the radius R, as $\Gamma \propto R$ (Meszaros & Rees, 1993). When the internal energy of the fireball is completely converted into kinetic energy, the acceleration phase is completed and the highest Lorentz factor Γ_{i} is reached. Afterwards, the so called coasting phase begins, in which the shell is moving with approximately constant Lorentz factor Γ_{i}. As the radius of the shell increases, the shell sweeps up more and more matter of the circumburst medium and an external shock is created. When the blast wave sweeps up enough matter of the circumburst medium, the blast wave starts to substantially decelerate. The mass m of the material which is swept up from the external medium by the blast wave, in the distance R from the central engine, is calculated by

$$m(R) = 4\pi \int_0^R r^2 \rho_{\text{ext}}(r) dr = 4\pi K \int_0^R r^{2-k} dr = \frac{4\pi K}{3-k} R^{3-k}. \tag{52}$$

At the so called deceleration radius R_{dec}, the initial energy of the shell E_1 equals the swept up relativistic energy of the external medium m, i.e

$$m\left(R_{\text{dec}}\right) = \frac{E_1}{c^2 \Gamma_0^2}. \tag{53}$$

By combining Equation (52) and (53), it follows for the deceleration radius R_{dec} that

$$R_{\text{dec}} = \left(\frac{3-k}{4\pi K} \frac{E_1}{c^2 \Gamma_{\text{i}}^2} \right)^{1/(3-k)}, \tag{54}$$

as in Panaitescu & Kumar (2000).

Due to relativistic effects of an object moving in the direction of the observer, the radius R and the observer time t are connected by the following equation,

$$t = \frac{R}{c_t \Gamma_{\text{i}}^2 c} \tag{55}$$

where c_t is a numerical value which can vary depending on the details of the hydrodynamic evolution of the blast wave (Sari, 1997). For the coasting phase, when Γ is constant, c_t equals 2. To describe a decelerating source, c_t has to be set to a higher value between 4 and 7 depending on the assumption of a radiative or adiabatic blast-wave.

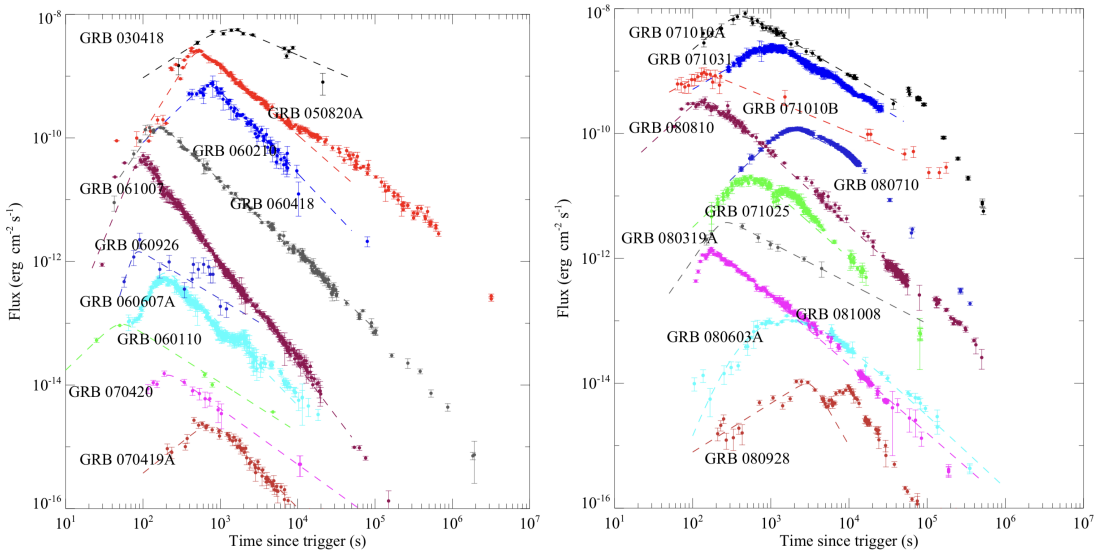

Figure 9: Early optical afterglow light-curves of a sample of GRBs with a dominating forward shock component. The forward shock peak is clearly visible. Figure taken from Gao et al. (2015).

A photon emitted at the deceleration time t_{dec} is observed at

$$t_{\mathrm{dec}} = \frac{t_{\mathrm{peak_1}}}{1+z}, \tag{56}$$

where z is the obtained redshift of the GRB. The time $t_{\mathrm{peak_1}}$ equals the time of the first peak which can be observed in many GRB afterglow light-curves (see Fig. 9). Finally, by connecting the Equations (54), (55) with $c_{\mathrm{t}} = 2$ and (56), one obtains for the time of the forward shock peak

$$t_{\mathrm{peak_1}} = \frac{1+z}{2c\Gamma_{\mathrm{i}}^2}\left(\frac{3-k}{4\pi m_{\mathrm{p}} n R_{\mathrm{ref}}^k}\frac{E}{c^2\Gamma_{\mathrm{i}}^2}\right)^{1/(3-k)} \tag{57}$$

and for the Lorentz factor

$$\Gamma_{\mathrm{i}}(t_{\mathrm{peak_1}}) = \left(\left(\frac{1+z}{2ct_{\mathrm{peak_1}}}\right)^{(3-k)}\frac{3-k}{4\pi m_{\mathrm{p}} n R_{\mathrm{ref}}^k}\frac{E}{c^2}\right)^{1/(8-k)}. \tag{58}$$

For a homogeneous circumburst medium ($k = 0$), it follows

$$\Gamma_{\mathrm{i}}(t_{\mathrm{peak_1}}) = \left(\frac{3E(1+z)^3}{32\pi n m_{\mathrm{p}} c^5 t_{\mathrm{peak_1}}^3}\right)^{1/8}, \tag{59}$$

as in Molinari et al. (2007).

After the deceleration time, most of the fireball's energy is transformed into the the accelerated interstellar medium kinetic energy and the shock evolution can be described by the self-similar solution of Blandford & McKee (1976), which is summarized in the following. For a thin and homogeneous spherical shell, the conserved internal energy E of the blast wave, which is released in a full sphere, is given by

$$E = \frac{4\pi}{3-k} K R^{3-k}\Gamma^2 c^2, \tag{60}$$

with $K = m_{\mathrm{p}} n R_{\mathrm{ref}}^k$ the normalization constant of the wind profile medium (Piran, 2004). The Sedov length l is given by

$$l = \left(\frac{(3-k)E}{Kc^2}\right)^{\frac{1}{3-k}}, \tag{61}$$

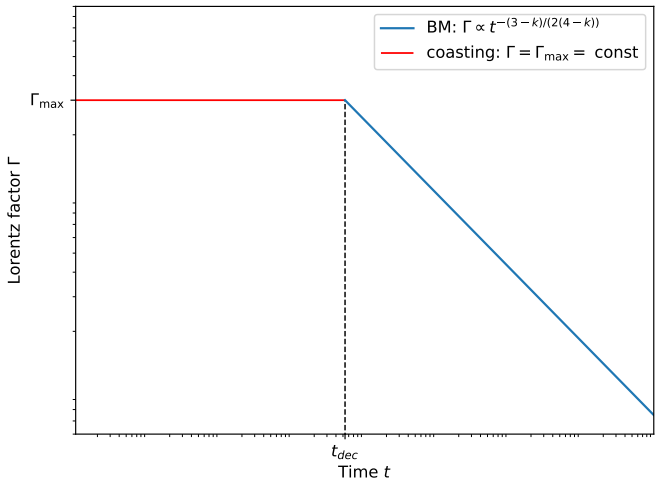

Figure 10: Evolution of the Lorentz factor Γ of a blast wave after the acceleration phase in log-log scale. During the coasting phase, Γ is approximately constant until the deceleration time $t_{\rm dec}$. After the coasting phase, the shell is decelerating and the evolution of Γ can be described with the Blandford & McKee (BM) solution.

which corresponds to the radius, at which the blast wave becomes approximately Newtonian ($\Gamma \approx 1$). Thus, the Blandford-McKee (BM) solution is only valid in the region $R_{\rm dec} < R \ll l$. Similar to Piran (2004), one obtains the relations for the evolution of the Lorentz factor and the radius of the blast wave as a function of time by connecting the Equations (60), (61) and (55),

$$R(t) = \left(\frac{c_{\rm t} c l^{3-k}}{4\pi}\right)^{1/(4-k)} t^{1/(4-k)}, \tag{62}$$

$$\Gamma(t) = \left(\frac{l^{3-k}}{4\pi c^{3-k} c_{\rm t}^{3-k}}\right)^{1/2(4-k)} t^{-(3-k)/(2(4-k))}. \tag{63}$$

When the blast wave propagates into the ISM with $k = 0$, the equations describing the evolution of the blast wave can be simplified to

$$R(t) = 3.2 \times 10^{16} E_{52}^{1/4} n_1^{-1/4} t_{\rm s}^{1/4} {\rm cm}, \tag{64}$$

$$\Gamma(t) = 260 E_{52}^{1/8} n_1^{-1/8} t_{\rm s}^{-3/8}, \tag{65}$$

where E_{52} is the energy in units of 10^{52} erg, n_1 is the ISM density in ${\rm cm}^{-3}$ and $t_{\rm s}$ is the time in seconds (Sari, 1997). The evolution of the Lorentz factor Γ during the coasting and deceleration phase is shown in Figure 10.

When the shock slows to the non-relativistic regime ($\Gamma \ll 1$), its motion can be described by the Sedov-Taylor solution. This regime is not expected to be reached in the time scale of the light-curves which are obtained during this study and thus is not discussed here.

3.2 Duration of the collision

The total duration Δt_c of the collision corresponds to the time the forward shock needs to cross the first decelerating shell and is given by

$$\Delta t_c = \frac{\Delta R_1(t_c)}{\beta_{fs} - \sqrt{1 - \Gamma_1(t_c)^{-2}}}, \tag{66}$$

where β_{fs} is the velocity of the forward shock created when the second shell collides with the first shell. $\Delta R_1(t_c)$ is the width and $\Gamma_1(t_c)$ the Lorentz factor of the shock front of the first shell at the time of collision.

The width of the first shell ΔR_1 at the time of collision can be obtained by

$$\Delta R_1(t_c) = \frac{V}{4\pi {R_c}^2} \tag{67}$$

for a spherical symmetric shell and the radius of the collision R_c. The volume V of the shell can be calculated by using the global conservation of energy, momentum and mass (Equation (48)).

In the frame of the first shell, the Lorentz factor of the forward shock which is created when the second shell collides with the first shell, is approximately given by

$$\Gamma'_{fs} = \sqrt{2}\Gamma_{rel}, \tag{68}$$

where $\Gamma_{rel} = (1 - \beta'^2_{rel})^{-1/2}$ is the Lorentz factor with which the second shell moves relative to the first shell (Blandford & McKee, 1976). The relative velocity β'_{rel} can be computed by performing a Lorentz transformation from the frame of the central engine to the frame of the first shell, e.g.

$$\beta'_{rel} = \frac{\beta_2 - \beta_1}{1 - \beta_2\beta_1}, \tag{69}$$

where $\beta_1 = (1 - \Gamma_1(t_c)^{-2})^{1/2}$ and $\beta_2 = (1 - (\Gamma_2)^{-2})^{1/2}$ are the velocities of the first and the second shell in the central engine frame. Finally, to obtain the velocity of the forward shock in the central engine frame, a Lorentz transformation back to the laboratory frame of $\beta'_{fs} = (1 - (\Gamma'_{fs})^{-2})^{1/2}$ is needed, which yields

$$\beta_{fs} = \frac{\beta'_{fs} + \beta_1}{1 + \beta'_{fs}\beta_1}. \tag{70}$$

3.3 Produced heat energy during the collision

An estimate for the heat energy E_{heat} during the collision can be obtained by analyzing energy and momentum conservation during the collision. The energy conservation yields

$$m_1(t_c)\Gamma_1(t_c) + m_2\Gamma_2 = \left(m_1(t_c + \Delta t_c) + m_2 + \frac{E_{heat}}{c^2}\right)\Gamma_m, \tag{71}$$

where $m_1(t_c)$ and m_2 are the masses and $\Gamma_1(t_c)$ and Γ_2 the Lorentz factors of the two shells at the time of the beginning of the collision. Γ_m is the Lorentz factor of the merged shell after the collision at $t_c + \Delta t_c$. As a result of the second shell propagating into empty space, the mass $m_2 = E_2/(c^2\Gamma_2^2)$, the Lorentz factor Γ_2 and thus, also the velocity $\beta_2 = (1 - \Gamma_2^{-2})^{1/2}$ of the second shell are constant and correspond to the initial values. From momentum conservation, it follows that

$$m_1(t_c)\Gamma_1(t_c)\beta_1(t_c) + m_2\Gamma_2\beta_2 = \left(m_1(t_c + \Delta t_c) + m_2 + \frac{E_{heat}}{c^2}\right)\Gamma_m\beta_m. \tag{72}$$

Equations (71) and (72) can be combined to identify the values of the two unknown parameters, the energy E_{heat} which is converted into heat during the collision, and the Lorentz factor of the merged shell Γ_m. The equations cannot be solved analytically and thus, numerical methods are needed.

4 Modeling process of GRB lightcurves

Before the beginning of the simulations, a set of input parameters has to be fixed. A list of all input parameters of the model of Straub (2019) can be found in Appendix A with a short explanation. In the following, the multi-dimensional parameter space of the model is analyzed. To fit the simulated light-curves to the measured GRB light-curves, it is necessary to investigate the parameter space and the impact of individually changing each parameter on the simulations. An extensive parameter study of the model is presented in Chapter 4.1. To obtain physical meaningful parameters and to reduce the large parameter space, as many input parameters as possible are connected to observable parameters of a GRB. The used approach is explained in Chapter 4.2.

4.1 Parameter study of the model

For the parameter study, the two cases for the external medium, the ISM with $k = 0$ and the wind profile medium with $k = 2$, were considered separately. Additional to the density n, there is another input parameter for the external medium with a wind profile, the radius R_{ref}, which adds one more degree of freedom and hence complicates the simulations. The parameters describing the physical setting at the shock front are the electron spectral index p, the fraction of energy which is converted into the electrons ϵ_{e} and the portion which is converted into the creation of a magnetic field ϵ_{B}. The first blast wave is characterized by its kinetic energy E_1 and its initial Lorentz factor Γ_{i} and radius R_{i}. As the first shell sweeps up almost all circumburst matter, the second shell is moving into empty space with constant Lorentz factor Γ_2 until it collides with the first shell. In addition to the Lorentz factor, the second shell is characterized by its width ΔR_2 and its energy E_2. The time of collision is defined by the Lorentz factor of the first shell at the time of collision $\Gamma_1(t_{\mathrm{c}})$.

Parameter	**Fixed value**
p	2.5
ϵ_{B}	0.001
ϵ_{e}	0.01
n	1 cm^{-3}
E_1	5×10^{53} erg
Γ_{i}	100
R_{i}	2×10^{17} cm
$\Gamma_1(t_{\mathrm{c}})$	30
E_2	3×10^{54} erg
Γ_2	35
ΔR_2	1×10^{14} cm

(a) $k = 0$ (ISM)

Parameter	**Fixed value**
p	2.5
ϵ_{B}	0.005
ϵ_{e}	0.05
n	0.1 cm^{-3}
R_{ref}	1×10^{17} cm
E_1	5×10^{53} erg
Γ_{i}	200
R_{i}	2×10^{17} cm
$\Gamma_1(t_{\mathrm{c}})$	30
E_2	1×10^{53} erg
Γ_2	70
ΔR_2	1×10^{12} cm

(b) $k = 2$ (wind profile)

Table 1: Chosen values which were fixed for the parameter study for the ISM case with $k = 0$ (a) and the wind profile medium with $k = 2$ (b), for which one more parameter R_{ref} has to be set to normalize the external medium density.

In order to better understand the influence of each input parameter on the simulated light-curves, each parameter was changed while the others were fixed to values in typical dimensions. In Table 1 the chosen parameters which were fixed before the beginning of the parameter study are listed. The dependency of the simulated light-curves on all input parameters are shown in Figures 11 and

12 for the ISM case with constant density and $k = 0$ and for the external medium with wind profile and $k = 2$ in Figures 13 and 14. It is important to stress that in the model of Straub (2019), the evolution of the blast wave is calculated only for the BM phase, so after the deceleration time, when self-similarity is meaningful. Thus, the early simulated light-curve is not meaningful because the computation of the hydrodynamics is only valid after the forward shock peak. Therefore, confident interpretations about the simulated light-curves can be only made after the maximum of flux of the first peak.

As expected, the higher the fraction of the energy which is converted into the creation of a magnetic field (ϵ_B) and into the electrons at the shock front (ϵ_e), the more synchrotron radiation is produced and thus, the higher is the observed flux in the simulated light-curve. A change of ϵ_B or ϵ_e is ambiguous and thus, these parameters cannot be distinguished or fit individually. The density n scales the amount of radiation which is produced in a similar way to ϵ_B and ϵ_e. The collision of the first blast wave with the circumburst medium is stronger the more particles there are which can be accelerated at the external shock front. In addition, the larger the density is, the faster the first shell decelerates to lower Lorentz factors and thus, the earlier the Lorentz factor $\Gamma_1(t_\mathrm{c})$ is reached. Thus, the higher the density of the external medium, the earlier is the beginning of the collision of both shells. For the case $k = 2$, a change of the density n and the normalizing radius R_ref cannot be distinguished and can therefore only be fit together. The electron index p is the only parameter which changes the steepness of the decline of the light-curve far after the forward shock peak in the BM deceleration phase which is consistent with the model of Granot & Sari (2002). In the model of Granot & Sari (2002), the flux is described by a power law with an index which is only dependent on p.

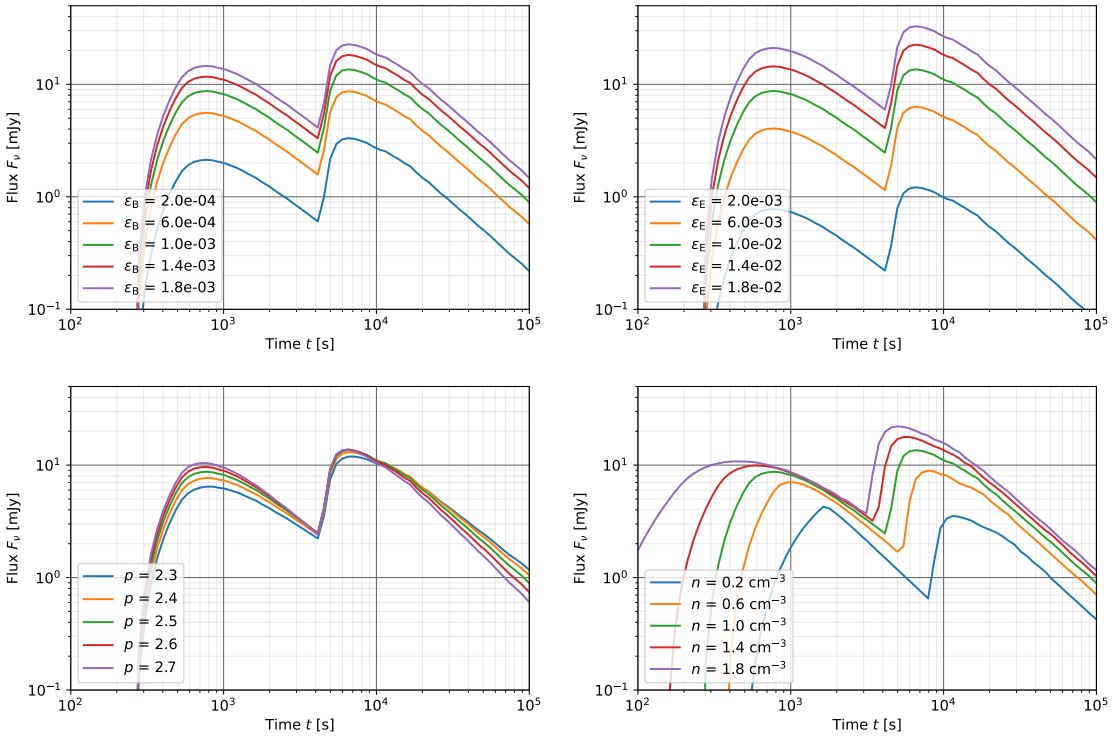

Figure 11: The dependencies of the simulated light-curve on the the microphysical parameters ϵ_B ϵ_e and p and the density n of the ISM with $k = 0$.

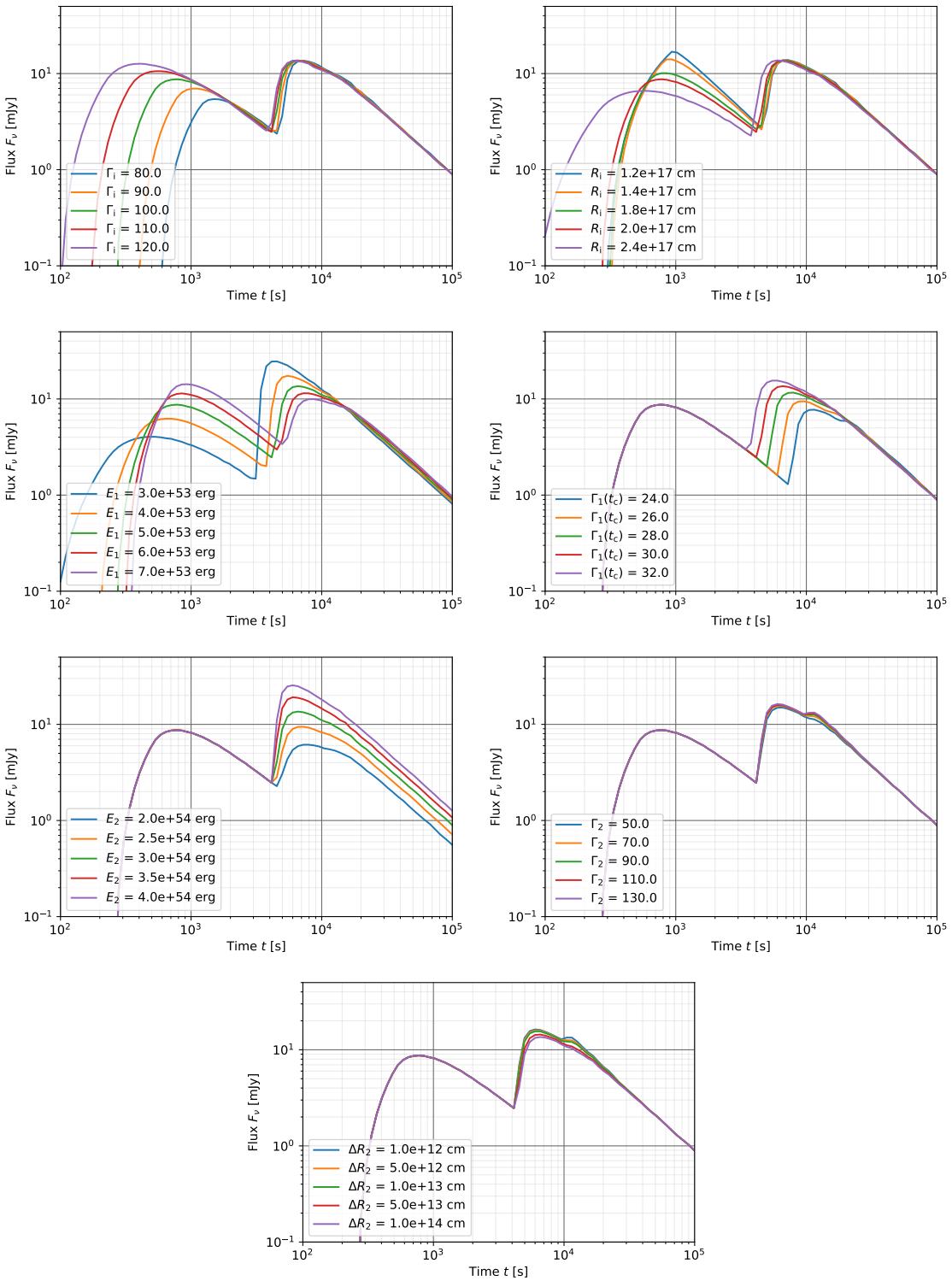

Figure 12: The dependencies of the simulated light-curve on the parameters of the initial Lorentz factor Γ_i and radius R_i and the kinetic energy E_1 of the first shell. The time of collision is determined by the Lorentz factor of the first shell at the time of collision $\Gamma_1(t_\mathrm{c})$. In addition, the impact of the energy E_2, the Lorentz factor Γ_2 and the width ΔR_2 of the second shell on the produced radiation during the collision is shown.

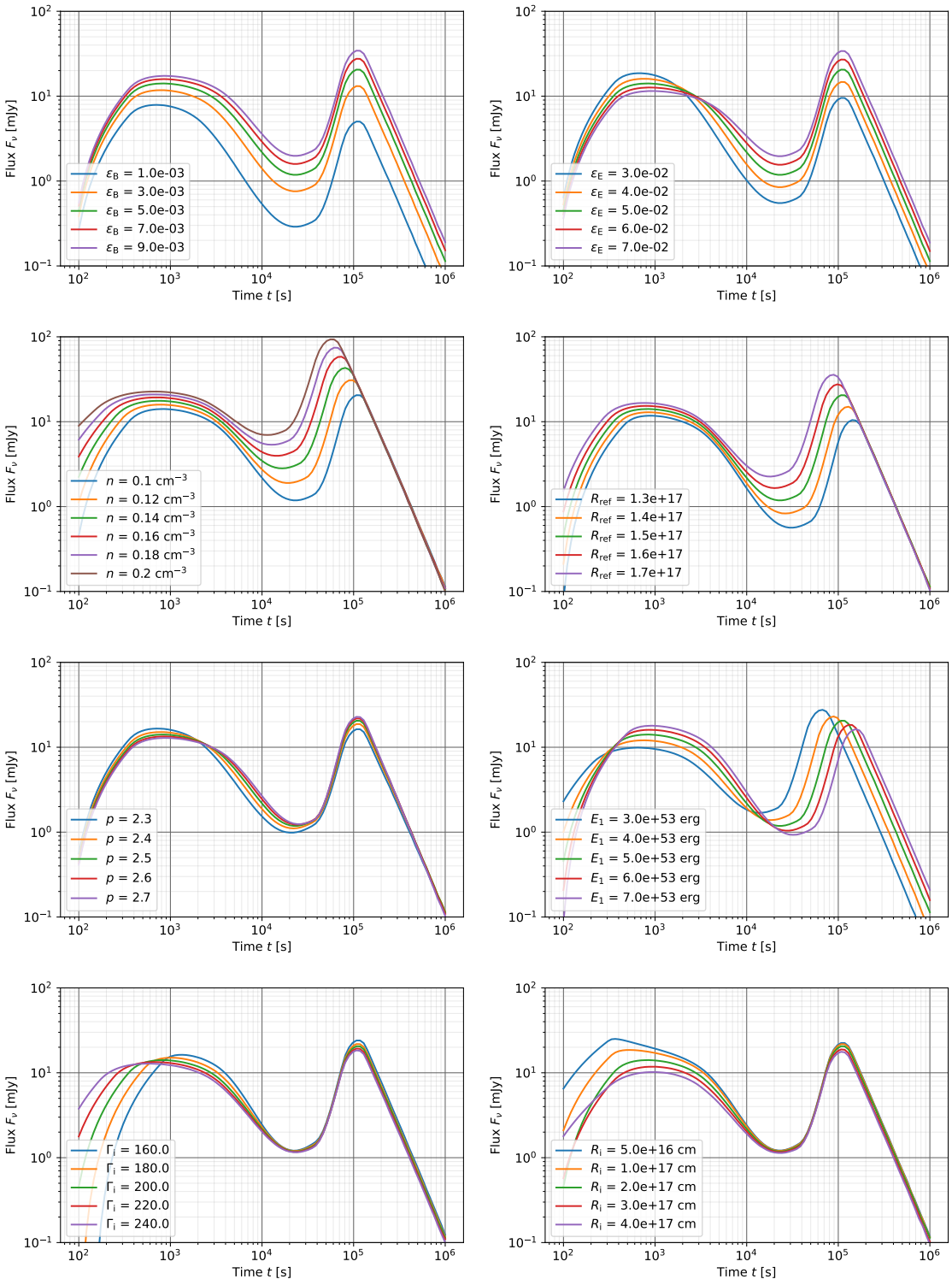

Figure 13: The dependencies of the simulated light-curve on the the microphysical parameters ϵ_B and ϵ_e. The density n of the external medium with $k = 2$ is normalized by the additional parameter R_{ref}. In addition, the impact of the electron index p, the kinetic energy of the first shell E_1, the initial Lorentz factor Γ_i and the radius R_i of the first shell on the simulated light-curves is shown.

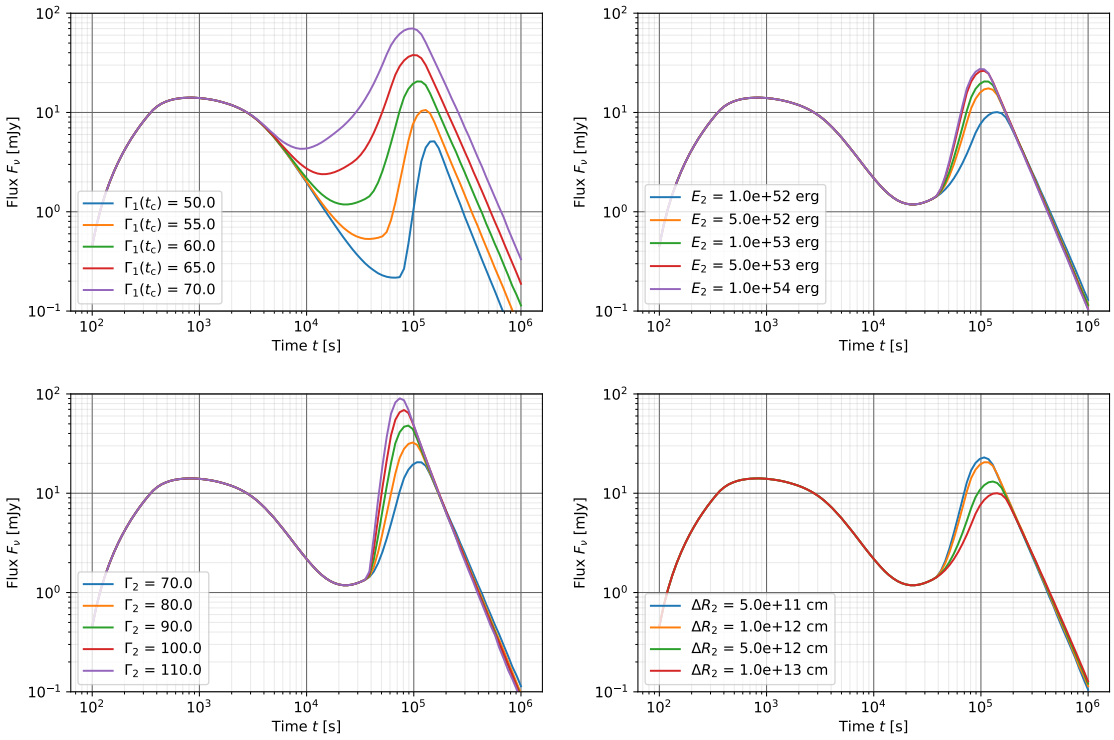

Figure 14: The dependencies of the simulated light-curve on the Lorentz factor of the first shell at the time of collision $\Gamma_1(t_c)$, the energy E_2, the Lorentz factor Γ_2 and the width ΔR_2 of the second shell for the case of two colliding shells in an external medium with $k = 2$.

Furthermore, a higher kinetic energy E_1 of the first blast wave allows for more energy to be converted into radiation and the simulated flux of the forward shock peak is higher. With a higher kinetic energy, the first shell decelerates slower to $\Gamma_1(t_c)$ and thus the beginning of the collision is later if the energy of the first blast wave is higher (see Equation (65)). Contrary to the forward shock peak, the jump component becomes smaller in proportion to the first peak with increasing E_1. The smaller the energy of the first shell E_1, the smaller is the Lorentz factor $\Gamma_1(t_c)$, and therefore more internal energy is freed during the collision. If at a fixed radius R_i, the corresponding initial Lorentz factor Γ_i is set to a higher value, the BM region is reached in an ISM ($k = 0$) at an earlier time with the decay of the light-curve beginning earlier, and hence more radiation is produced during the external shock. If the same Lorentz factor Γ_i is set to be reached at a larger radius R_i, the collision with the ISM becomes softer. Therefore, less radiation is produced and the BM region is reached later. In contrast to the external medium with a wind profile, R_i is a very sensitive parameter in the ISM case and already small variations of R_i can change the shape of the early light-curve. In the wind case scenario, the blast wave is surrounded by a large number of particles at early times when the radius is small. In order for the blast wave to penetrate the dense matter, the initial Lorentz factor has to be set to a much higher value than in the ISM case to produce the same amount of radiation. The Lorentz factor of the second shell Γ_2 has to be increased too in comparison to the ISM case, so that the second shell is able to collide with the first shell. The time of the collision is determined by the Lorentz factor $\Gamma_1(t_c)$, as expected. The earlier the collision is, the more radiation is produced because the collision is stronger. In the ISM case, the magnitude of the jump component is only dependent on the energy of the second shell. The higher the energy of the second shell E_2 is, the stronger the collision is and hence, the more radiation is produced during the collision. The Lorentz factor Γ_2 and the width ΔR_2 of the second shell have a small impact on the size of the jump. By increasing the Lorentz factor Γ_2 or decreasing the width ΔR_2, a second peak becomes visible which originates from the reverse shock created during the collision. A second hump in the jump component is not visible in the wind case scenario because the peaks are expected to overlap. Thus, in the wind case scenario, an increase of Γ_2 or a smaller width

ΔR_2 increases the magnitude of the jump. As expected, the parameters describing the second shell and the collision (Γ_2, E_2, ΔR_2, $\Gamma_1(t_c)$) are not changing the shape of the forward shock peak because the second shell is moving into empty space and is thus not creating any radiation before the collision.

4.2 Comparison to numerical model

A similar, but fully numerical and more complex model for the late collision of two shells in the GRB afterglow phase was created in previous work by Vlasis et al. (2011). The hydrodynamic equations and the equations describing the dynamics of the blast waves and shocks were solved by using the Adaptive Mesh Refinement version of the Versatile Advection Code (AMRVAC) (Meliani et al., 2007; Keppens et al., 2003). The hydrodynamic model was coupled to the radiation code of van Eerten & Wijers (2009), which is also used during this thesis. In the numerical model of Vlasis et al. (2011), not only the case of an isotropic explosion as in the model of Straub (2019) is considered but also the more likely jet scenario characterized by its jet opening angle. Additional to light-curves, snapshots of the hydrodynamic profile of the shells during the collision and emission images of different parts of the fluid were simulated.

Case	Γ_2	E_2
1	$\Gamma_i/\sqrt{2}$	E_1
2	$2\Gamma_i/\sqrt{2}$	E_1
3	$\Gamma_i/\sqrt{2}$	$2E_1$
4	$2\Gamma_i/\sqrt{2}$	$2E_1$

Table 2: Values for the Lorentz factor Γ_2 and the energy E_2 of the second shell as a function of the initial Lorentz factor $\Gamma_i = 23$ and the energy $E_1 = 10^{52}$ erg of the first shell for the four cases as described in Vlasis et al. (2011).

For the simulated light-curves in Vlasis et al. (2011), a circumburst medium with constant density $n = 1$ cm^{-3} and $k = 0$ was considered. The initial Lorentz factor was set to $\Gamma_i = 23$ at radius $R_i = 2.04 \times 10^{17}$ cm and the energy of the first shell to $E_1 = 10^{52}$ erg. Four different cases for the energy and the Lorentz factor of the second blast wave are distinguished, which are summarized in Table 2. The width of the second shell was chosen to be $\Delta R_2 = 3 \times 10^{13}$ cm. The electron spectral index was set to the typical value of 2.5 and the parameters ϵ_B and ϵ_e to 0.01 and 0.1 respectively. The optical light-curves which were simulated in Vlasis et al. (2011), are shown in Figure 15. One result of Vlasis et al. (2011) was that the jet opening angle has a high impact on the resulting light-curve. The smaller the jet opening angle the steeper is the flux rise. The case of an isotropic explosion without a jet is marked with a red dotted line in Figure 15.

The parameter combination of Vlasis et al. (2011) was tested with the model created by Straub (2019). The simulated light-curves are shown in Figure 16. The BM phase of the light-curve begins with the chosen parameter set only after 10 days and thus, the model of Straub (2019) can only reproduce meaningful light-curves after this time. Therefore, the simulation of a collision at 0.2 days as in Figure 15 is not possible to simulate with the model of Straub (2019). Instead, a small value for $\Gamma_1(t_c) = 8$ had to be chosen to obtain a graph, in which the collision occurs in the BM region, where the model can solve the hydrodynamics correctly. Consequently, as the $\Gamma_1(t_c)$ is much smaller than the chosen Γ_2, the second reverse shock peak becomes exceptionally large, which is not an observed phenomenon.

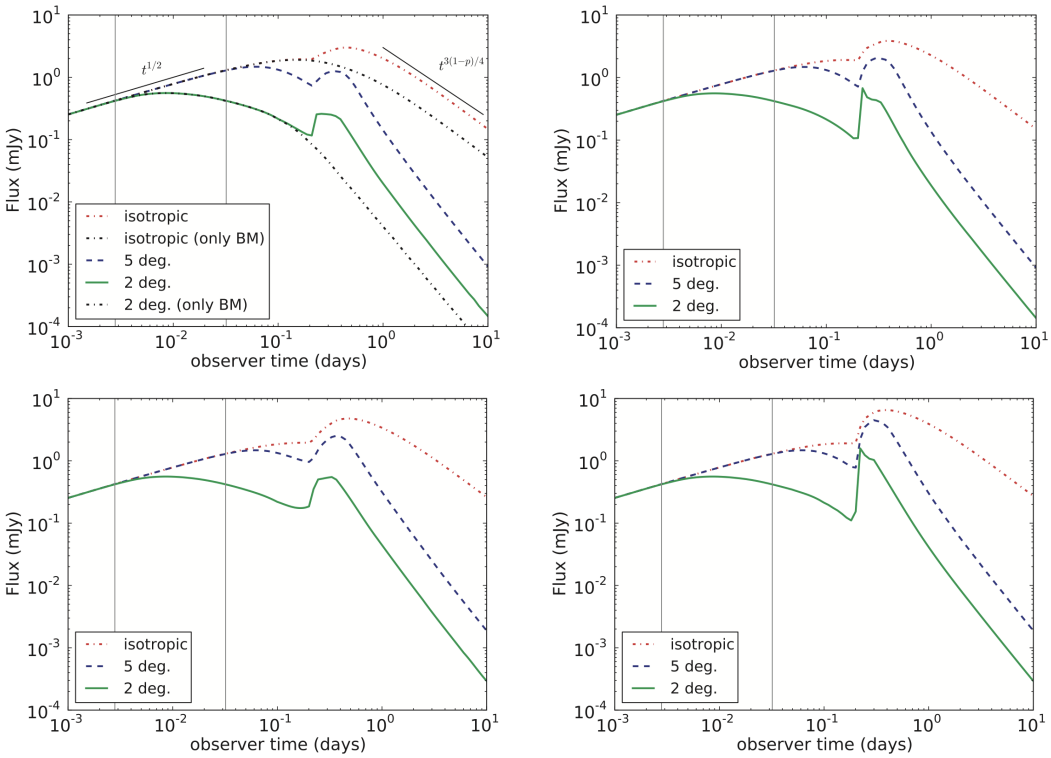

Figure 15: Simulated optical light-curves of Vlasis et al. (2011) for different jet opening angles. Case 1 (top left): $\Gamma_2 = \Gamma_i/\sqrt{2}$, $E_2 = E_1$. Case 2 (top right): $\Gamma_2 = 2\Gamma_i/\sqrt{2}$, $E_2 = E_1$. Case 3 (bottom left): $\Gamma_2 = \Gamma_i/\sqrt{2}$, $E_2 = 2E_1$. Case 4 (bottom right): $\Gamma_2 = 2\Gamma_i/\sqrt{2}$, $E_2 = 2E_1$.

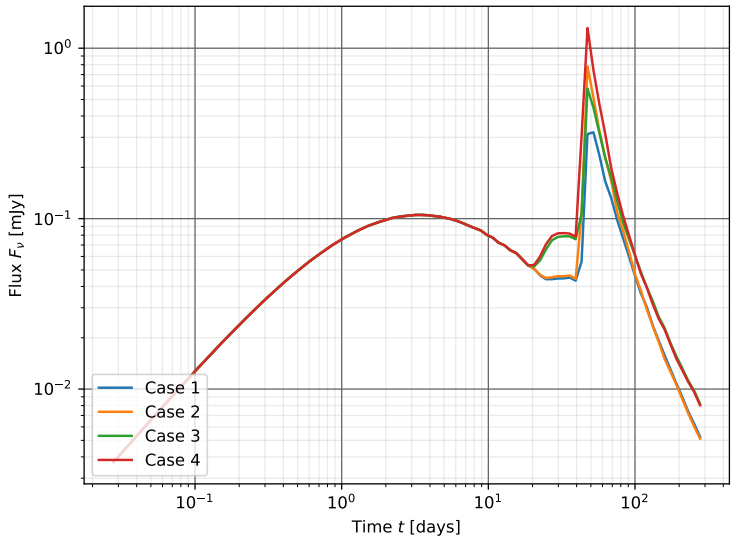

Figure 16: Simulated optical light-curves with the model of Straub (2019) for the four cases of Vlasis et al. (2011) as in Figure 15.

The Lorentz factor of the first shell at the time of collision can be estimated by Equation (76) which yields $\Gamma_1(t_c = 0.2 \text{ days}) \approx 36$ for $E_2 = 2E_1 = 2 \times 10^{52}$ erg. The Lorentz factor $\Gamma_2 = 2\Gamma_i/\sqrt{2} \approx 33$ is smaller than $\Gamma_1(t_c)$ which is not physically meaningful as a collision does not occur. As a collision still occurs with the chosen parameter set for Vlasis et al. (2011), the dynamics of the shells are differently described in both models. As the parameter combinations tested in Vlasis et al. (2011) are arbitrarily chosen without physical motivation, it is not possible to compare the chosen parameter set with the model used during this thesis.

During the parameter study obtained in Section 4.1, it was shown that the energy of the second shell E_2 strongly influences the peak of the jump component (see Figure 12), which is qualitatively consistent with the modeled light-curves of Vlasis et al. (2011), i.e. the difference in the amplitude of the jump component between case 1 and 3, and case 2 and 4 in Figure 15. In contrast to the model of Vlasis et al. (2011), the amplitude of the jump component is weakly dependent on the Lorentz factor of the second shell Γ_2 in the model of Straub (2019) (see Figure 12).

4.3 Connection of input and observable parameters

At first, the parameters which were measured for the specific GRB, e.g. the redshift z and the corresponding luminosity distance D_L have to be set. The luminosity distance D_L can be computed from the redshift z. The redshift of GRBs is primarily determined by finding characteristic absorption features in spectra of the optical afterglow. From 2043 GRBs, which were observed between 1997 and 2019, for only 522 could the redshift be determined, which corresponds to a rate of around 25 % [1].

Additionally, the parameters describing the physical setting at the shock front have to be chosen. Meaningful values for these parameters can only be obtained from SEDs which are compared to theoretical models. In the following, the advanced model by Granot & Sari (2002) is used, in which also the case of an external medium with a wind profile is considered. The different possible synchrotron spectra can be found in Appendix B. In general the density of the external medium is given by Equation (7). The evolution of the break frequencies with time gives the best evidence for the differentiation between an ISM with $k = 0$ and an external medium with a wind profile. How much synchrotron radiation is produced in a relativistic shock is dependent on the strength of the magnetic field, the energy of the accelerated electrons at the shock front and the characteristics of the circumburst medium. In the used radiation model of van Eerten (2010), it is assumed that the electrons are accelerated at the shock front to a power-law distribution of Lorentz factor γ_e (see Equation (2)) with an index p. A fraction ϵ_e of the shock energy is transferred to the electrons (see Equation (3)) and another fraction ϵ_B to the creation of a magnetic field described by Equation (4). As the fraction of energy going into the electrons and into the magnetic field cannot exceed the shock energy, ϵ_e and ϵ_B have to satisfy the condition that $\epsilon_B + \epsilon_e < 1$. The electron index p can be extracted from the measured spectral slopes in the power law segments (see Fig. 2). A typical value for the electron index is $p = 2.5$. Once one of the five theoretical spectra of Granot & Sari (2002) is chosen which best fits the observed SEDs, constraints on the spectral break frequencies can be extracted. By using the equations for the break frequencies and the corresponding flux from Table 2 of Granot & Sari (2002), the constraints can be translated directly into conditions for the microphysical parameters ϵ_B, ϵ_e, the density n and the kinetic energy E_1 of the first blast wave.

The first peak originating from the forward shock is only dependent on the properties of the first blast wave. Thus, the parameters describing the first shell, the microphysical parameters of the shock front and the external medium can be obtained at first by deactivating the propagation of the second shell and fitting the simulated light-curves to the data. Thereafter, the evolution of the second shell can be added and the parameters describing the properties of the second shell and the collision can be obtained.

The first blast wave is characterized by its kinetic energy E_1, its initial Lorentz factor Γ_i and the corresponding radius R_i. The strategy to obtain physical meaningful parameters and to reduce the

[1] Statistics from `http://www.mpe.mpg.de/~jcg/grbgen.html`

number of free input parameters to as few as possible, is to connect observable parameters with input parameters of the model. In some GRB afterglow light-curves, the observations were started so early that the peak of the forward shock is visible (see Fig. 9). If the forward shock peak is visible in the light-curve, the initial Lorentz factor Γ_i can be calculated by using Equation (58) as a function of the measured time of the forward shock peak t_peak. The corresponding initial radius R_i can be set to the deceleration radius, which can be calculated by using Equations (55) and (56),

$$R_\mathrm{i} = R_\mathrm{dec} = 2c\Gamma_\mathrm{i}^2 \frac{t_\mathrm{peak}}{1+z}. \tag{73}$$

For GRBs with a redshift z, the isotropic energy release E_iso can be calculated by

$$E_\mathrm{iso} = \frac{4\pi D_\mathrm{L}^2 S}{1+z}, \tag{74}$$

assuming an isotropic emission of energy. Here, S is the fluence and D_L the luminosity distance. The fluence S is the integral over the best-fit power-law spectrum of the GRB. From the isotropic energy release E_iso, it is possible to estimate the kinetic energy of the blast wave E by assuming an efficiency η for the conversion of the energy E into radiation, e.g.

$$E_\mathrm{iso} = \eta E. \tag{75}$$

Thus, there is a lower limit on the kinetic energy E_1. There is no specific value for the efficiency η but in practice, it is often set to 10% (Kobayashi et al., 1997).

The dimension of the Lorentz factor of the first shell at the time of collision $\Gamma_1(t_\mathrm{c})$ can be estimated by using the Blandford & McKee solution (Equation (65)) and by using Equation (56) for the redshift correction, which yields

$$\Gamma_1(t_\mathrm{c}) = \left(\frac{(3-k)E}{4\pi c^{5-k} 5^{3-k} m_\mathrm{p} n R_\mathrm{ref}^k}\right)^{1/2(4-k)} \left(\frac{t_\mathrm{c}}{1+z}\right)^{-(3-k)/(2(4-k))}. \tag{76}$$

Here, t_c is the time of collision in the observer frame, which can be set to the start of the sudden late flux rise in the light-curve. The numerical value was chosen to be $c_\mathrm{t} = 5$.

5 Results for GRB 100621A

At first, the parameters which were determined by observations for GRB 100621A are set. As the measured SEDs were in conflict with the wind scenario ($k = 2$) (Greiner et al., 2013), only the ISM case ($k = 0$) is considered in the following. By assuming a typical radiative efficiency of 10% and the measured value of $E_{\mathrm{iso}} = (2.8 \pm 0.3) \times 10^{52}$ erg, the kinetic energy of the blast wave can be calculated by Equation (75) yielding $E = (2.8 \pm 0.3) \times 10^{53}$ erg, which corresponds to the dark blue points in Figure 6. In the following three of the six dark blue grid points of Figure 6 are chosen to test the model,

a) $n = 1\ \mathrm{cm}^{-3}, \epsilon_{\mathrm{B}} = 5.62 \times 10^{-4}, \epsilon_{\mathrm{e}} = 1.78 \times 10^{-2}$,
b) $n = 10\ \mathrm{cm}^{-3}, \epsilon_{\mathrm{B}} = 5.62 \times 10^{-5}, \epsilon_{\mathrm{e}} = 3.16 \times 10^{-2}$,
c) $n = 100\ \mathrm{cm}^{-3}, \epsilon_{\mathrm{B}} = 5.62 \times 10^{-6}, \epsilon_{\mathrm{e}} = 5.62 \times 10^{-2}$.

The choice of the three cases is arbitrary and serves only as illustration. For other radiative efficiencies, there are other valid parameter combinations. For each case a) to c), the initial Lorentz factor Γ_{i} can be calculated by equation 58. For GRB 100621A, the peak of the forward shock is at $t_{\mathrm{peak}_1} = (380 \pm 30)$ s (Greiner et al., 2013). The peak time t_{peak_1} can be only determined with a high uncertainty because of the underlying flares at that time. The radius R_{i} can be set to the corresponding deceleration radius, which can be computed by using Equation (73).

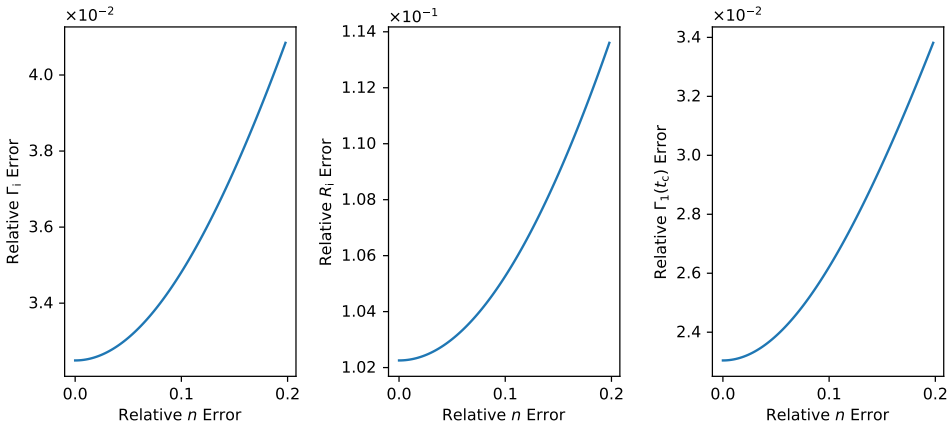

Figure 17: Error propagation of the calculated input parameters as a function of the relative uncertainty of the density for $n = 10$.

To estimate the uncertainties of the parameters which are calculated as a function of the observable parameters, i.e. Γ_{i}, R_{i} and $\Gamma_1(t_{\mathrm{c}})$, the uncertainties of the literature parameters (E_{iso}, t_{peak_1}, t_{c}) and the density n are needed. As the uncertainty of n is unknown and unable to be uniquely determined, a conservative estimate of the relative error is taken to be 20% in the following. The error propagation of a general function $f(x_i)$ is calculated as

$$f = \prod_{i=1}^{n} x_i^{b_i} \implies \left(\frac{\delta f}{f}\right)^2 = \sum_{i=1}^{n} b_i^2 \left(\frac{\delta x_i}{x_i}\right)^2 . \tag{77}$$

In Figure 17, the error propagation of Γ_{i} (Equation (58), R_{i} (Equation (73)) and $\Gamma_1(t_{\mathrm{c}})$ (Equation (76)) are calculated as a function of the relative error of the density n. Even for a large relative error in density n of 20%, the relative errors of the Lorentz factors Γ_{i} and $\Gamma_1(t_{\mathrm{c}})$ are of order 4% and for R_{i} of the order 11%.

For the three cases, the Lorentz factor Γ_{i} and the radius R_{i} are constrained to the following values,

a) $\Gamma_{\mathrm{i}} = 104 \pm 4$, $R_{\mathrm{i}} = (16.0 \pm 1.8) \times 10^{16}$ cm,
b) $\Gamma_{\mathrm{i}} = 78 \pm 3$, $R_{\mathrm{i}} = (9.0 \pm 1.0) \times 10^{16}$ cm,
c) $\Gamma_{\mathrm{i}} = 59 \pm 2$, $R_{\mathrm{i}} = (5.1 \pm 0.6) \times 10^{16}$ cm.

By fixing the redshift to the measured value of $z = 0.542$ for GRB 100621A (Milvang-Jensen et al., 2010) and the luminosity distance to the corresponding value $D_L = 9.74 \times 10^{27}$ cm, all parameters are set which are necessary to describe the radiation which is produced by one blast wave decelerating into an ISM. The simulated light-curves for the three cases (a) to (c) are shown in Figure 18. The flux of the host galaxy of 0.08 mJy was added as a factor to all following simulations. As expected, all three light-curves are similar, which shows that the implemented radiation model of van Eerten & Wijers (2009) is in agreement with the model of Granot & Sari (2002). The modeled flux function of the canonical afterglow for the J band given by Equation G of Table 2 in Granot & Sari (2002) is shown in the right panel of Figure 18 as the pink dashed line. The model of Granot & Sari (2002) fits the observed data and also the corresponding simulated light-curves of Straub (2019) well.

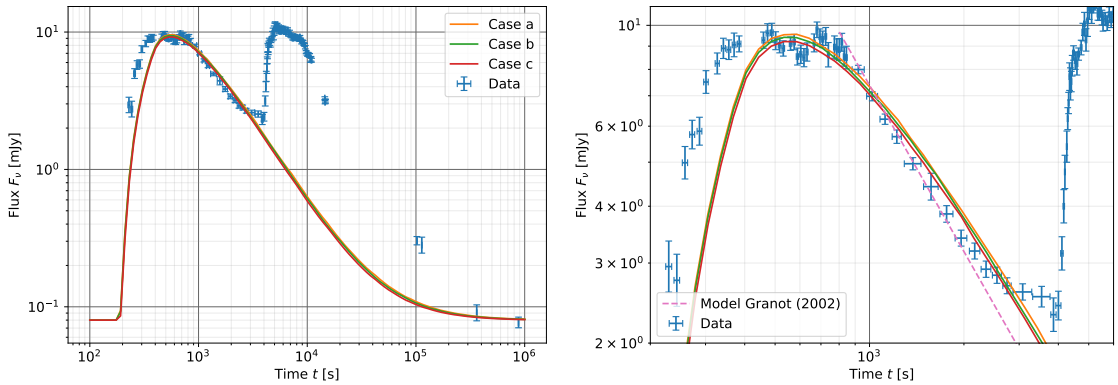

Figure 18: Simulated light-curves for $E_1 = 2.8 \times 10^{53}$ erg and the three illustrative cases (a), (b) and (c), which all yield a similar light-curve, as expected (right panel is a zoom of the left). Cases a, b and c belong to the following parameter combinations
Case a: $n = 1\ \mathrm{cm}^{-3}, \epsilon_B = 5.62 \times 10^{-4}, \epsilon_e = 1.78 \times 10^{-2}, \Gamma_i = 104, R_i = 16.01 \times 10^{16}$ cm,
Case b: $n = 10\ \mathrm{cm}^{-3}, \epsilon_B = 5.62 \times 10^{-5}, \epsilon_e = 3.16 \times 10^{-2}, \Gamma_i = 78, R_i = 9.01 \times 10^{16}$ cm,
Case c: $n = 100\ \mathrm{cm}^{-3}, \epsilon_B = 5.62 \times 10^{-6}, \epsilon_e = 5.62 \times 10^{-2}, \Gamma_i = 59, R_i = 5.06 \times 10^{16}$ cm.

The time of collision was measured for GRB 100621A at around $t_c = 4.0 \pm 0.2$ ks from which the Lorentz factor of the first shell at the time of collision can be calculated by Equation (76) for the cases (a) to (c),

a) $\Gamma_1(t_c) = 30.5 \pm 1.0$,
b) $\Gamma_1(t_c) = 22.9 \pm 0.8$,
c) $\Gamma_1(t_c) = 17.2 \pm 0.6$.

By using the results of the parameter study discussed in Chapter 4, it is possible to estimate the dimension of the other free parameters. As a second peak in the jump component was not observed in the GRB 100621A light-curve, the parameters have to be chosen such that the reverse shock peak is suppressed in the simulated light-curves. Therefore, the width of the second shell is set to a large value $\Delta R_2 = 10^{14}$ cm and the Lorentz factor of the second shell Γ_2 to a small value but under the condition that the Lorentz factor Γ_2 is larger than Γ_c because otherwise the shells do not collide. The amplitude of the jump component is then only dependent on the energy of the second shell, which was scaled up until the jump component was in the same dimension as the measured flux increase. The results for the first attempt for the optimal choice of parameters for the cases a) to c) are shown in Figure 19. The simulated light-curves fit the observations already surprisingly well. Only at late times after the collision, the light-curve declines faster than observed but with the same slope. After the collision, the hydrodynamics are described by a combined shell with energy $E_1 + E_2$. As a simplification, the energy which was radiated away was not subtracted from the energy of the combined shell $E_1 + E_2$ and is likely the reason for the higher simulated flux. The energy of the second shell E_2 is in all three cases approximately 1.6×10^{54} erg.

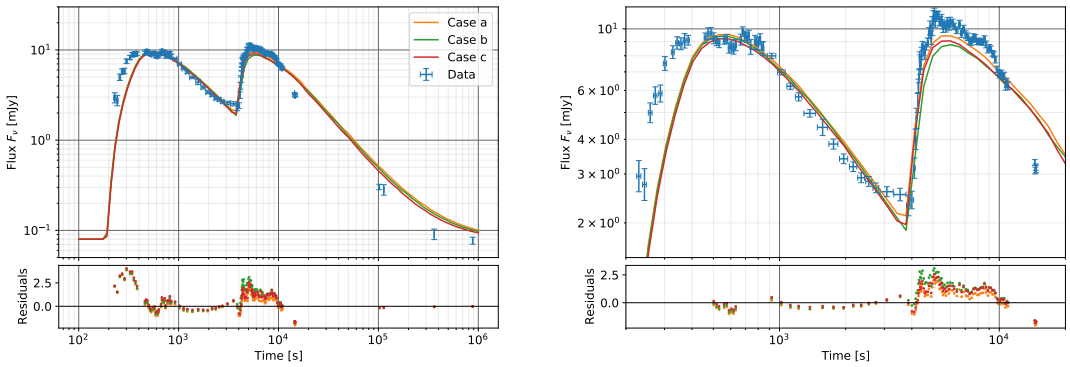

Figure 19: Simulated light-curves for the initial choice of the input parameters for the simulations of GRB 100621A (right panel is a zoom of the left). Parameters for $n, \epsilon_B, \epsilon_e, \Gamma_i, R_i$ are chosen as described in the text for the three cases a) to c) and as shown in Figure 18. The following parameters for the collision and the second shell were set
Case a: $\Gamma_1(t_c) = 30.5, \Gamma_2 = 34, E_2 = 1.6 \times 10^{54}$ erg, $\Delta R_2 = 10^{14}$ cm,
Case b: $\Gamma_1(t_c) = 22.9, \Gamma_2 = 26, E_2 = 1.6 \times 10^{54}$ erg, $\Delta R_2 = 10^{14}$ cm,
Case c: $\Gamma_1(t_c) = 17.2, \Gamma_2 = 20, E_2 = 1.6 \times 10^{54}$ erg, $\Delta R_2 = 10^{14}$ cm.

The simulated light-curves with the initial estimate of the parameter values have the following χ^2 values:

a) $\chi^2 = 14$,
b) $\chi^2 = 26$,
c) $\chi^2 = 17$.

For the calculation of the χ^2 value, only the data after the forward shock peak and not affected by flares were included.

In the following, another parameter study was performed to determine how much a variation of each parameter changes the light-curve with the aim to improve the fit. The parameter studies are shown in Appendix C for each case. The values for the different parameters for each case were chosen as shown in Figure 18 and 19. During the parameter study, only one of the parameters was varied and the light-curves were simulated.

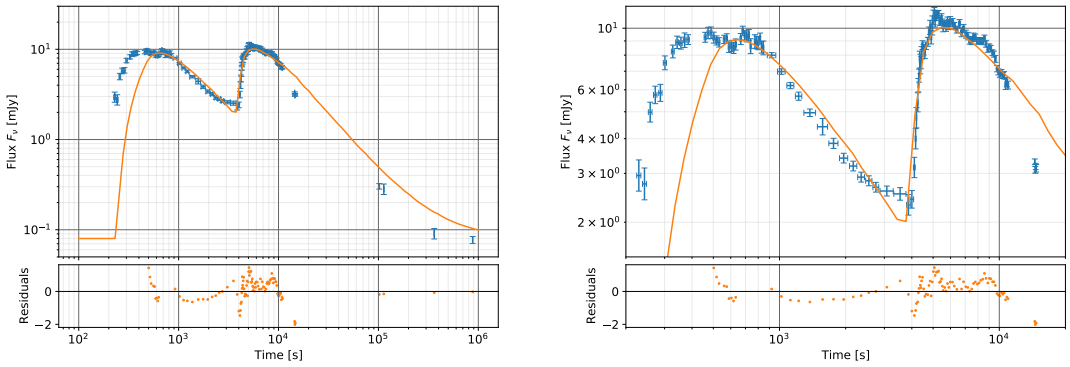

Figure 20: Best fit plot obtained when varying all parameters around the initially chosen values in case a) as described in the text (right panel is a zoom of the left). The parameters of the best fit are $E_1 = 2.7 \times 10^{53}$ erg, $n = 0.9$, $\Gamma_i = 102$, $R_i = 1.5 \times 10^{17}$ cm, $\Gamma_1(t_c) = 30$, $E_2 = 1.6 \times 10^{54}$ erg, $\Gamma_2 = 30$, $\Delta R_2 = 1.0 \times 10^{14}$ cm. The fit gives a χ^2 value of 10.

By choosing a grid of parameter values around the initial estimated values, the best fit for case a) was searched. The best fit was obtained by the simulation with the smallest χ^2 value. The final best fit is shown in Figure 20. The χ^2 value for the best fit is 10 with the following parameters:

- $E_1 = 2.7 \times 10^{53}$ erg,
- $n = 0.9$,
- $\Gamma_\mathrm{i} = 102$
- $R_\mathrm{i} = 1.5 \times 10^{17}$ cm,
- $\Gamma_1(t_\mathrm{c}) = 30$,
- $E_2 = 1.6 \times 10^{54}$ erg,
- $\Gamma_2 = 30$,
- $\Delta R_2 = 1.0 \times 10^{14}$ cm.

The simulated light-curve fits the data, particularly in the jump component, very accurately. The change of the χ^2 value is not significantly large, which emphasizes the accuracy of the initially estimated parameter values, which could be obtained easily by evaluating the parameter study in Section 4.1.

6 Conclusion and Outlook

The simple hydrodynamics model created by Straub (2019) coupled to the radiation code of van Eerten (2010) reproduces the data of GRB 100621A surprisingly well. With a good choice of parameters, it is possible to model the decrease of the GRB light-curve after the forward shock peak and the jump component. The observation of jump components in GRB afterglows allow one to learn more about the origin of GRBs and their central engine. The jump component is an additional tool which allows the determination of characteristic parameters of the relativistic shells such as the Lorentz factor and energy. Whilst it is not possible to determine the Lorentz factor of the first shell and the Lorentz factor of the second shell directly from the simulations, the model still allows one to constrain the parameter space and to make statements about their relation. It was found that the Lorentz factor of the second shell Γ_2 has to be small and in the dimension of the Lorentz factor of the first shell at the time of collision $\Gamma_1(t_c)$. The result is surprising as rebrightenings measured in the prompt emission of GRBs are often considered to be originating from shells with a high Lorentz factor $\Gamma \sim 10^2 - 10^3$ (Ruffini et al., 2018). It was found that the amplitude of the jump component is mostly dependent on the energy of the second blast wave. From the extensive first parameter study obtained in Section 4.1, it was possible to produce an accurate initial guess for all parameters. After a second parameter study, it was possible to reduce the χ^2 value of the initial estimate from 14 to $\chi^2 = 10$ for case a).

During this thesis, the focus was to find physically motivated parameters as input for the hydrodynamic simulations. The peak of the forward shock was used to calculate the initial Lorentz factor Γ_i and radius R_i. For GRBs with an observed rebrightening for which the observations began after the expected forward shock peak (e.g. GRB 081029 (Nardini et al., 2011)), the method of Molinari et al. (2007) for calculating the initial Lorentz factor is not applicable and there exist two additional free parameters which complicate the simulations. Additionally, constraints on the parameters n, ϵ_B and ϵ_e can only be obtained when it is possible to identify the type of synchrotron spectrum of Granot & Sari (2002), the break frequencies and their evolution, for which extensive broadband observations at different times are required.

To make confident statements about the generality of the parameter relations, it is necessary to test the model also for other GRBs, e.g. GRB 081029 (Nardini et al., 2011) or GRB 100814A (Nardini et al., 2014). Furthermore, there may exist other observable parameters which might be used in future work to connect measurable parameters with model parameters, for example the duration of the collision (equation 66) and the produced heat energy. In order to obtain a better fit of the simulated light-curve to the measured data at early times before the BM region and at later times after the collision of both shells the model would need to be extended. Considering the simplicity of the model relative to the complexity of the phenomenon, most physical features are captured remarkably well.

7 Acknowledgments

I would first like to thank my thesis supervisor Dr. Jochen Greiner for the continuos encouragement and valuable guidance throughout the full time of my thesis. Additionally, I would like to pay my special regards to Dr. Damien Bégué for sharing his extensive expertise with me in many helpful discussions. I wish to acknowledge the support of my family, my boyfriend and friends, who always believed in me and kept motivating me.

References

Abbott B. P., et al., 2017, Physical Review Letters, 119, 161101

Blandford R. D., McKee C. F., 1976, Physics of Fluids, 19, 1130

Frederiks D. D., et al., 2013, The Astrophysical Journal, 779, 151

Galama T. J., et al., 1998, Nature, 395, 670

Gao H., Wang X.-G., Mészáros P., Zhang B., 2015, The Astrophysical Journal, 810, 160

Gehrels N., Piro L., Leonard P. J. T., 2002, Scientific American, 287, 84

Gehrels N., et al., 2004, The Astrophysical Journal, 611, 1005

Golenetskii S., et al., 2010, GRB Coordinates Network, 10882, 1

Granot J., Sari R., 2002, The Astrophysical Journal, 568, 820

Greiner J., et al., 2008, Publications of the Astronomical Society of the Pacific, 120, 405

Greiner J., et al., 2013, Astronomy and Astrophysics, 560, A70

Hjorth J., et al., 2003, Nature, 423, 847

Keppens R., Nool M., Tóth G., Goedbloed J. P., 2003, Computer Physics Communications, 153, 317

Klebesadel R. W., Strong I. B., Olson R. A., 1973, Astrophysical Journal, 182, L85

Kobayashi S., Piran T., Sari R., 1997, Astrophysical Journal, 490, 92

Kouveliotou C., Meegan C. A., Fishman G. J., Bhat N. P., Briggs M. S., Koshut T. M., Paciesas W. S., Pendleton G. N., 1993, Astrophysical Journal Letters, 413, L101

Krühler T., et al., 2011, Astronomy & Astrophysics, 534, A108

Lora-Clavijo F. D., Cruz-Perez J. P., Guzman F. S., Gonzalez J. A., 2013, arXiv e-prints, p. arXiv:1303.3999

Meliani Z., Keppens R., Casse F., Giannios D., 2007, Monthly Notices of the Royal Astronomical Society, 376, 1189

Mészáros P., 2006, Reports on Progress in Physics, 69, 2259

Meszaros P., Rees M. J., 1993, Astrophysical Journal, 405, 278

Metzger M. R., Djorgovski S. G., Kulkarni S. R., Steidel C. C., Adelberger K. L., Frail D. A., Costa E., Frontera F., 1997, Nature, 387, 878

Milvang-Jensen B., et al., 2010, GRB Coordinates Network, 10876, 1

Molinari E., et al., 2007, Astronomy and Astrophysics, 469, L13

Nardini M., et al., 2011, Astronomy & Astrophysics, 531, A39

Nardini M., et al., 2014, Astronomy & Astrophysics, 562, A29

Panaitescu A., Kumar P., 2000, The Astrophysical Journal, 543, 66

Piran T., 1999, Physics Reports, 314, 575

Piran T., 2004, Reviews of Modern Physics, 76, 1143

Rezzolla L., Zanotti O., 2013, Relativistic Hydrodynamics. Oxford University Press

Ruffini R., et al., 2018, The Astrophysical Journal, 852, 53

Sari R., 1997, The Astrophysical Journal, 489, L37

Sari R., Piran T., Narayan R., 1998, The Astrophysical Journal, 497, L17

Straub P., 2019, Bachelor thesis, Technical University Munich

Taub A. H., 1948, Physical Review, 74, 328

Ukwatta T. N., et al., 2010, GRB Coordinates Network, 10870, 1

Updike A., Nicuesa A., Nardini M., Kruehler T., Greiner J., 2010, GRB Coordinates Network, 10874, 1

Vlasis A., van Eerten H. J., Meliani Z., Keppens R., 2011, Monthly Notices of the Royal Astronomical Society, 415, 279

van Eerten H. J., 2010, PhD thesis, University of Amsterdam

van Eerten H. J., Wijers R. A. M. J., 2009, in Meegan C., Kouveliotou C., Gehrels N., eds, American Institute of Physics Conference Series Vol. 1133, American Institute of Physics Conference Series. pp 151–156 (arXiv:0902.0233), doi:10.1063/1.3155868

van Eerten H., van der Horst A., MacFadyen A., 2012, The Astrophysical Journal, 749, 44

Appendices

A Free parameters of the model

A.1 Observer position settings

Parameter	Parameter name in model	Meaning	Allowed Values
D_{L}	`r_obs`	Observer luminosity distance	> 0
z	`z`	Observer redshift	> 0

A.2 Parameters describing the physics setting

Parameter	Parameter name in model	Meaning	Allowed Values
ϵ_{B}	`epsilon_B`	Magnetic energy density behind the shock	$0 < \epsilon_{\mathrm{B}} < 1$
ϵ_{e}	`epsilon_E`	Fraction of the energy going into the electrons	$0 < \epsilon_{\mathrm{e}} < 1$
p	`p_synch`	Electron spectral index	> 2

A.3 Parameters describing the external medium

Parameter	Parameter name in model	Meaning	Allowed Values
k	`special_k`	Determines fluid profile of external medium (r^{-k})	$k = 0$ (ISM) $k = 2$ (wind profile)
n	`special_n_ref`	Particle proton density $\left[\frac{1}{\mathrm{cm}^3}\right]$; constant for $k = 0$, normalized with radius R_{ref} for $k = 2$	> 0
R_{ref}	`special_R_ref`	Used for normalization of the density of the external medium if $k = 2$; R_{ref} has no impact on the light curve if $k = 0$ [cm]	> 0

A.4 Parameters describing the shock front/ first shell

Parameter	Parameter name in model	Meaning	Allowed Values
R_{i}	`R_i`	Initial shock front radius (corresponds to `G_i`) [cm]	> 0
Γ_{i}	`G_i`	Initial Lorentz factor of the shock front for radiative simulations	> 0
E_1	`special_E_iso`	Total energy of the first blast wave [erg]	> 0

A.5 Parameters describing the collision with the second shell

Parameter	**Parameter name in model**	**Meaning**	**Allowed Values**
E_2	`E2`	Energy of the second shell [erg]	> 0
Γ_2	`G_2`	Lorentz factor of the second shell	> 0
$\Gamma_1(t_c)$	`G_c`	Lorentz factor of the first shell at the time of the collision	> 1
ΔR_2	`width2`	Width of the second shell [cm]	> 0

B Spectral model of Granot & Sari (2002)

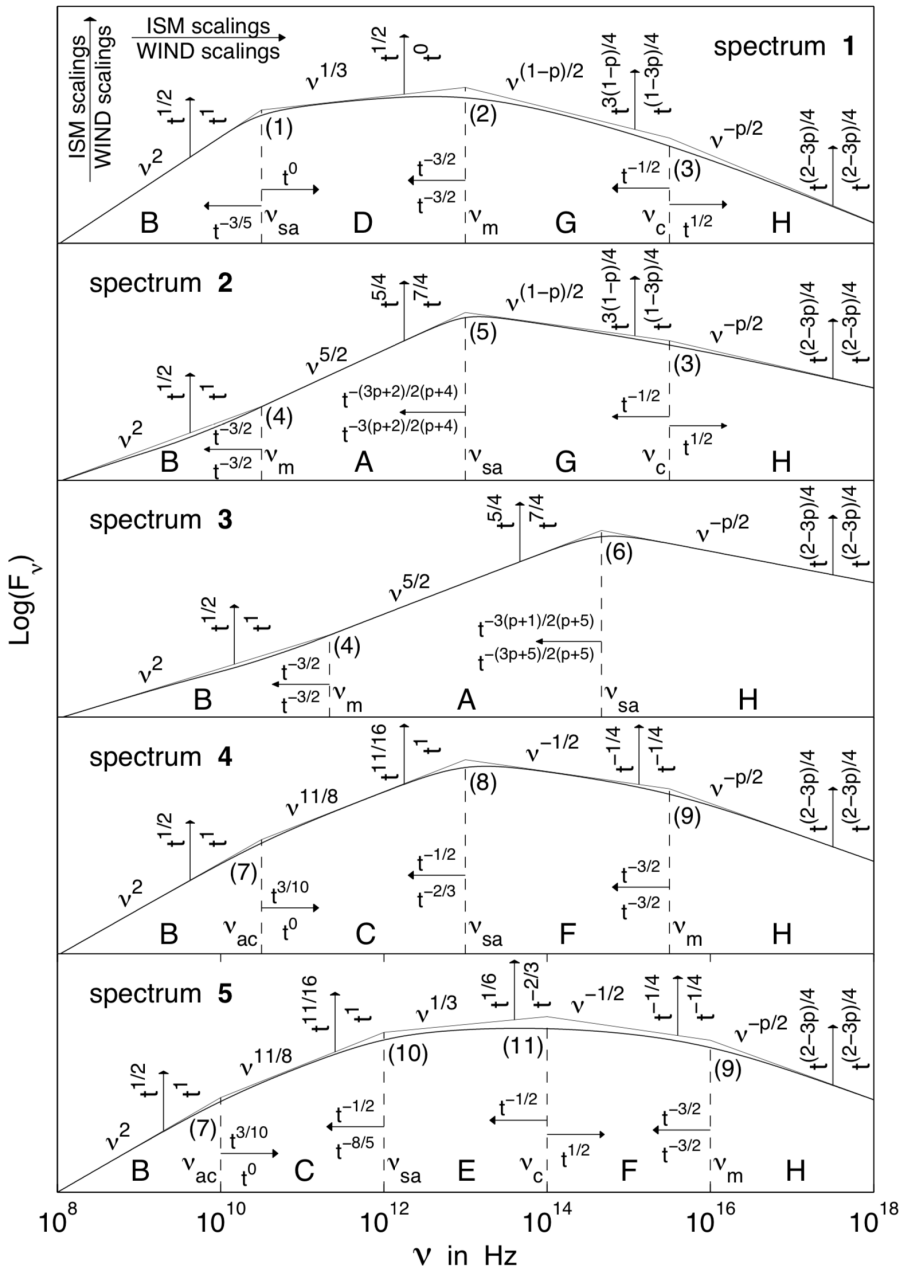

Figure 21: All possible broadband spectra which can be created by a relativistic blast wave accelerating electrons to a power law distribution with index p. The power-law segments are separated by specific break frequencies. The temporal scaling and evolution of the different break frequencies and segments are indicated by the relations above the arrow for the ISM (k=0) and below for the wind profile medium (k=2). Spectrum 1 and 2 belong to the slow cooling case ($\nu_\mathrm{m} < \nu_\mathrm{c}$), spectrum 4 and 5 to the fast cooling case ($\nu_\mathrm{c} < \nu_\mathrm{m}$). Figure taken from Granot & Sari (2002).

C Parameter study for cases (a) to (c) for GRB 100621A

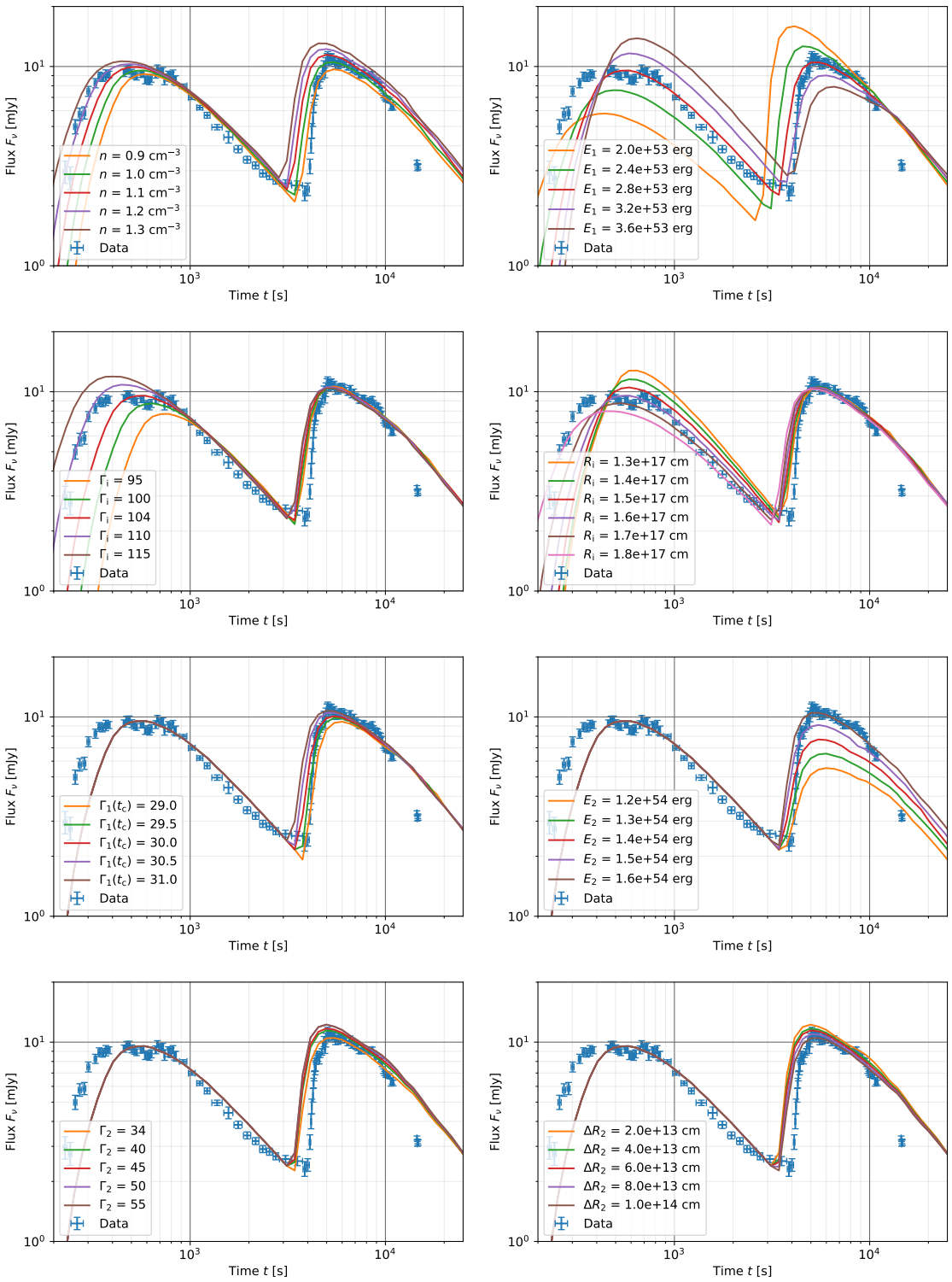

Figure 22: Parameter study for case a) for GRB 100621A. Only one parameter was changed in each plot while the other parameters were fixed. The values to which the parameters n, ϵ_B, ϵ_e, Γ_i and R_i were fixed, can be found in the text.

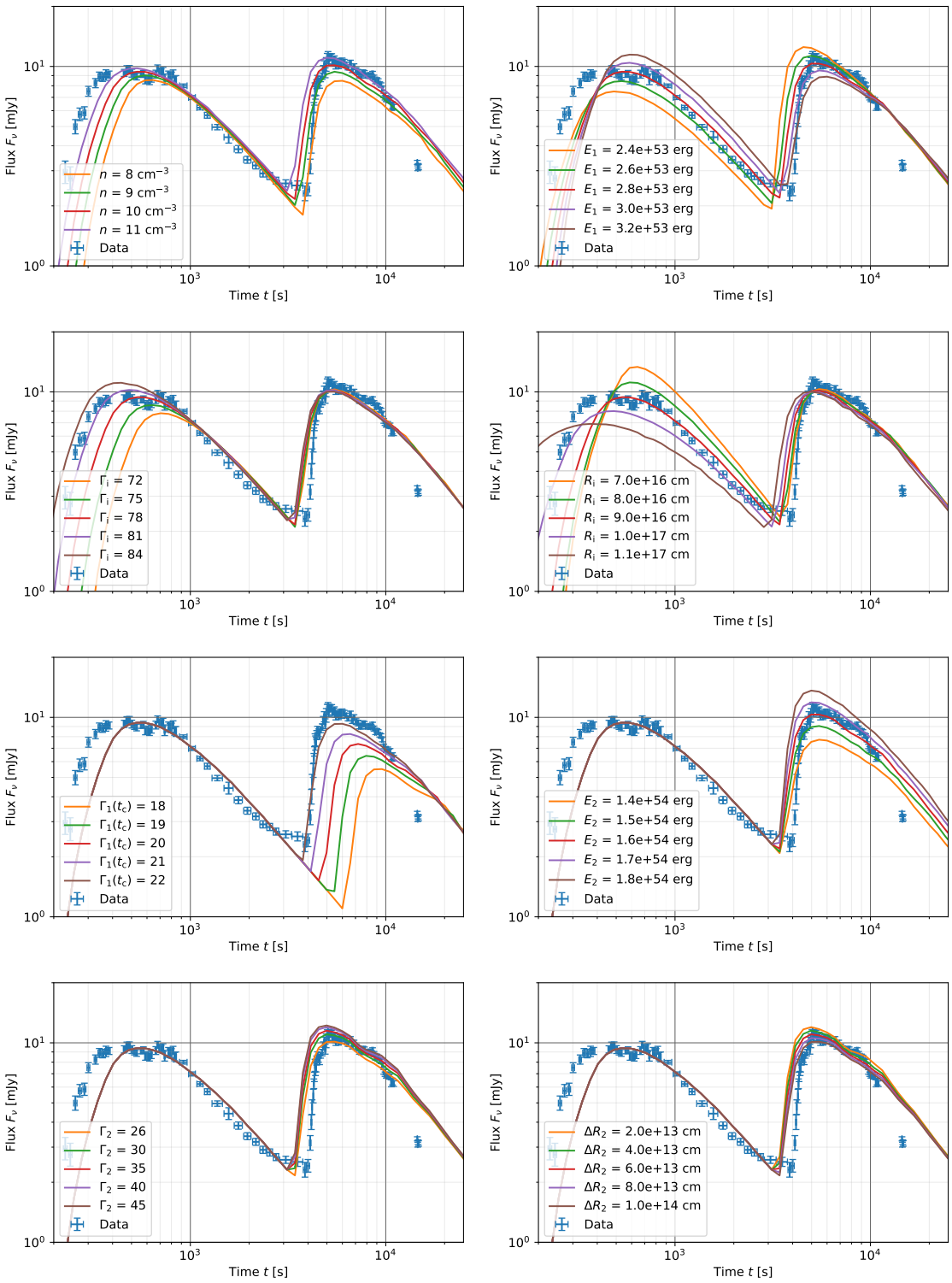

Figure 23: Parameter study for case b) for GRB 100621A. Only one parameter was changed in each plot while the other parameters were fixed. The values to which the parameters n, ϵ_B, ϵ_e, Γ_i and R_i were fixed, can be found in the text.

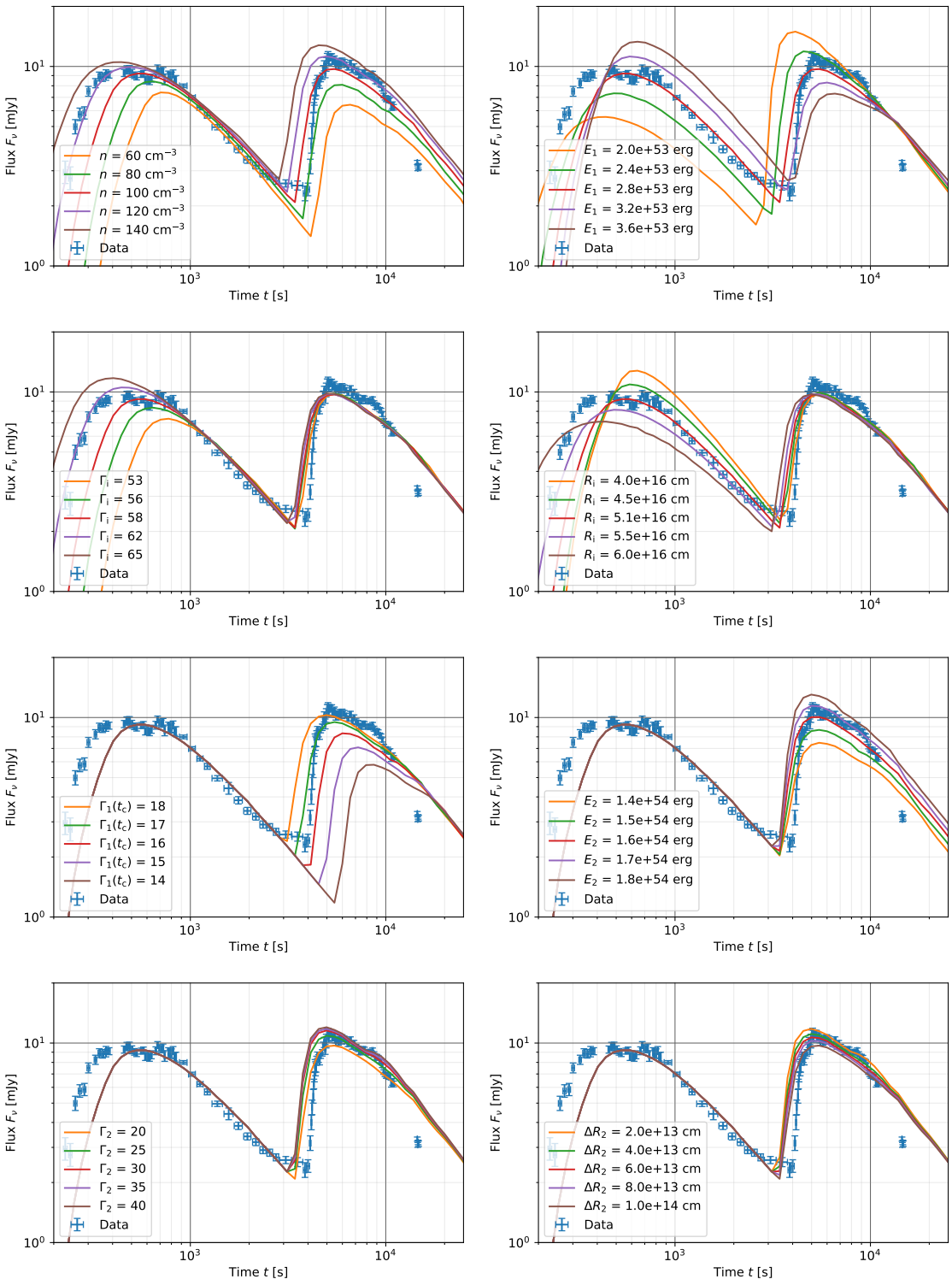

Figure 24: Parameter study for case c) for GRB 100621A. Only one parameter was changed in each plot while the other parameters were fixed. The values to which the parameters n, ϵ_B, ϵ_e, Γ_i and R_i were fixed, can be found in the text.